# Experimental study of the turbulent flow in a plane asymmetric diffuser

by

## Olle Törnblom

January 2003
Technical Reports from
Royal Institute of Technology
Department of Mechanics
SE-100 44 Stockholm, Sweden

Typsatt i LaTeX med mekaniks avhandlingsstil.

Akademisk avhandling som med tillstånd av Kungliga Tekniska Högskolan i Stockholm framlägges till offentlig granskning för avläggande av teknologie licentiatexamen onsdagen den 15:e januari 2003 kl 13.00 i Seminarierum S40, Teknikringen 8, Kungliga Tekniska Högskolan, Stockholm.

Universitetsservice US AB, Stockholm 2002

Olle Törnblom 2003 **Experimental study of the turbulent flow in a plane asymmetric diffuser**

Department of Mechanics, Royal Institute of Technology
SE-100 44 Stockholm, Sweden

## Abstract

The separating turbulent flow in a plane asymmetric diffuser is investigated experimentally. The considered flow case is suitable for fundamental studies of separation, separation control and turbulence modelling. The flow case has been studied in a specially designed wind-tunnel under well controlled conditions. The velocity field has been mapped out with PIV and LDV techniques in order to determine all three velocity components. Knowledge of all velocity components allows the formation of several quantities of interest in turbulence modelling such as the turbulence kinetic energy, the turbulence anisotropy tensor and the turbulence production rate tensor. Pressures are measured through the diffuser. The measured data will form a reference database which can be used for evaluation of turbulence models and other computational investigations. A comparative study is made where the measured turbulence data are used to evaluate an explicit algebraic Reynolds stress turbulence model (EARSM). A discussion regarding the underlying reasons for the discrepancies found between the experimental and the model results is made. A simple form of separation control using vortex generators is tested with positive result.

**Descriptors:** Fluid mechanics, wind-tunnel, turbulence, turbulence modelling, EARSM, asymmetric diffuser, boundary layer, PIV, LDV, vortex generator, control.

# Preface

This thesis is an experimental study of the turbulent flow in a plane asymmetric diffuser and it is based on the following papers.

**Paper 1.** Lindgren, B. Törnblom O. & Johansson, A. V. 2002 Measurements in a plane asymmetric diffuser with 8.5° opening angle. Part I: General flow characteristics. To be submitted.

**Paper 2.** Törnblom O., Lindgren, B. & Johansson, A. V. 2002 Measurements in a plane asymmetric diffuser with 8.5° opening angle. Part II: Comparison with model predictions for turbulence characteristics. To be submitted.

**Paper 3.** Törnblom O., Lindgren, B. & Johansson, A. V. 2002 Design and calibration of a plane asymmetric diffuser wind-tunnel.

## Division of work between paper authors

The papers included in this thesis have been written in collaboration with other researchers. Below follows a description of the contribution the respondent made to the different papers. Arne V. Johansson acted as supervisor and project leader in all investigations. The respondent made a major part of the writing of the papers, if not otherwise stated below.

**Paper 1.** This work was made in collaboration on equal terms with Björn Lindgren, who wrote the major part of the paper text. Parts of the work was presented at the 9th European Turbulence Conference, Southampton, UK, 2002 by the respondent and at the 11th International symposium on application of laser techniques to fluid mechanics, Lisbon, Portugal, 2002 by Björn Lindgren, with written contributions to the conference proceedings.

**Paper 2.** The experimental work was made in collaboration on equal terms with Björn Lindgren. The simulations were performed by Johan Gullman-Strand. Parts of the work was presented at the 9th European Turbulence Conference, Southampton, UK, 2002 by the respondent and at the 11th International symposium on application of laser techniques to fluid mechanics, Lisbon, Portugal, 2002 by Björn Lindgren, with written contributions to the conference proceedings.

**Paper 3.** The work was made in collaboration on equal terms with Björn Lindgren. Minor parts of the work has been presented at the 9th European Turbulence Conference, Southampton, UK, 2002 by the respondent and at the 11th International symposium on application of laser techniques to fluid mechanics, Lisbon, Portugal, 2002 by Björn Lindgren, with written contributions to the conference proceedings.

*Till minne av Morfar*

# Contents

**Preface** v
Division of work between paper authors v

**Chapter 1. Introduction** 1

**Chapter 2. Basic concepts** 4
2.1. Governing equations 4
2.2. Turbulent boundary layer separation 5
2.3. The plane asymmetric diffuser 7

**Chapter 3. Experiments** 8
3.1. Experimental facility 8
3.2. Measurement techniques 9
3.3. Results 11
3.4. Control 12

**Chapter 4. Concluding remarks and outlook** 14

**Acknowledgment** 15

**Bibliography** 16

**Papers**

**Paper 1: Measurements in a plane asymmetric diffuser with 8.5° opening angle. Part I: General flow characteristics** 21

**Paper 2: Measurements in a plane asymmetric diffuser with 8.5° opening angle. Part II: Comparison with model predictions for turbulence characteristics.** 49

**Paper 3: Design and calibration of a plane asymmetric diffuser wind-tunnel** 67

## CHAPTER 1

# Introduction

Fluid mechanics and fluid flow turbulence might (at a first glance) seem like narrow subjects, slightly detached from the world we live in, but I would say that it's quite the opposite. Liquid and gas flows are everywhere in our daily lives, as we are all living in the thin layer of gas covering the earth called the atmosphere. Whether we walk, cycle, go by car or take an airplane, we have to move through this layer of air, or rather, the air has to move around us. Even if we don't move at very high speed, it is likely that the flow around us will become turbulent (even when walking quickly one can hear the turbulent flow around the ears). Many other flows that we can find in our near environment for instance rivers, fires, chimney plumes and the wind blowing around a house are also turbulent, and many of the flows that we don't encounter as often such as inter-stellar gas clouds or the corona of the sun are turbulent too.

Turbulence is characterized by chaotic and three-dimensional motion of the fluid on a wide range of scales both in space and time. The chaotic and non-deterministic nature of turbulence makes it natural to analyze turbulence with statistical methods. Trying to exactly describe the velocity in every location at all times doesn't increase the understanding of turbulent flows. Instead, it is customary to study averages, standard deviations or higher order moments of the probability density functions for different flow quantities such as velocity, correlations between velocities in different directions or correlations between velocity and pressure. These correlations can be taken both in a single point or as a spatial correlation. A reason for studying these statistical quantities is that they all can be found in the governing equations (after some manipulation) and thus are important also in the mathematical modelling of turbulent flows. A flow becomes turbulent when the so called Reynolds number ($Re$) becomes large enough. The Reynolds number is a nondimensional measure of how large the inertia forces of the flow are compared to the viscous forces. Simply put, a high Reynolds number means that the viscosity of the flow is too small to be able to damp out flow disturbances. In turbulent flows, the Reynolds number determines the range of scales in space and time over which the kinetic energy will be spread out.

This thesis deals with incompressible flows, which means that the density of the fluid is assumed to be constant and not dependent on the pressure. The incompressibility assumption is valid for water and air flows at velocities that are small compared to the speed of sound in the respective medium. Air and water have another property in common, they are so called Newtonian fluids, which means that the relation between stress and strain-rate in the fluid is linear *i.e.* that the viscosity is constant with respect to the strain-rate. Under these conditions, air and water behave very much in the same way and their motions can be described by the same equations.

A fluid in relative motion to a solid object forms boundary layers in which the relative velocity between the fluid and the solid is gradually decreased until it is zero at the surface of the solid. This is called the no-slip boundary condition and it is valid for all flows considered in the present context. The velocity gradient in a boundary layer causes shearing of the fluid and shearing is a necessary ingredient for disturbance growth and for turbulence to occur and be sustained. Boundary layers are therefore one of the most important issues in fluid mechanics, without the no-slip condition this subject would be a lot less challenging.

A separating flow is the subject of this thesis. Separation occurs when the flow next to a solid surface is slowed down and eventually reversed, forming a region of circulating flow between the surface and the outer flow. Examples of situations where separation might occur and be of importance are; stall of wings at high angles of attack, in the rear end of bluff vehicles leading to increased air resistance and in bent channels in hydro power plants or ventilation systems leading to decreased performance. It is obvious that there are many benefits to earn from better knowledge of separation prediction and separation control. Separation can be divided into two groups depending on what caused the separation; geometry and pressure gradient induced separation. Geometry induced separation occurs in flows over objects with for example sharp corners where the acceleration of the flow would have to be infinite for it to follow the surface. Accordingly the separation point (the point where the separated region starts) is fixed at one position *i.e.* on the corner. In pressure gradient induced separation the deceleration of the flow next to the surface is a gradual process and the location of the separation point is determined by a balance between the inertia in the boundary layer and the adverse pressure gradient (the rate at which the pressure increases in the streamwise direction). This means that the prediction of the separation point is a much more complicated matter than in the case with geometry induced separation.

Predicting a turbulent flow means solving the governing equations for the flow, but this quickly becomes an impossible task as the Reynolds number, and thus the range of scales, is increased. For practically all flow cases, the governing equations have to be solved numerically, but not even the most powerful supercomputers of today have a chance of exactly solving for instance the flow around a car or an airplane. This is because the number of variables needed to resolve the smallest turbulent scales increases with Reynolds number as $Re^{9/4}$.

The alternative, if solving the problem with a computer isn't an option, is to make an experiment, this has been the traditional way of testing fluid dynamic design. Many experiments are costly though, and some things such as automatic optimization are easier to do with a computer than in an experiment. Therefore, turbulence models are used in order to circumvent the problem of increasing computational effort with increasing Reynolds number. In large-eddy simulations (LES), only the largest scales of the flow are computed directly, and the effects of smaller scales are modelled using the large scales as input to the model. In engineering applications, the dominating approach is still to consider only time- (or ensemble-) averaged momentum equations, complemented with evolution equations for some set of turbulence quantities, in order to close the whole set of equations (see chapter 2).

Accurate prediction of separating flows is one of the major challenges for turbulence models, and the measurements presented in this thesis were made both to give a well defined test case and to add detailed knowledge about where the models need to be improved. A future task is to elucidate possible routes towards separation control methods.

CHAPTER 2

# Basic concepts

## 2.1. Governing equations

The flow considered in this thesis and many other flows at moderate speed can be described by the incompressible Navier-Stokes equations,

$$\frac{\partial \tilde{u}_i}{\partial t} + \tilde{u}_j \frac{\partial \tilde{u}_i}{\partial x_j} = -\frac{1}{\rho}\frac{\partial \tilde{p}}{\partial x_i} + \nu \frac{\partial^2 \tilde{u}_i}{\partial x_j \partial x_j} \tag{2.1}$$

$$\frac{\partial \tilde{u}_i}{\partial x_i} = 0. \tag{2.2}$$

Cartesian tensor notation has been used when the above equations were formulated and Einstein's summation convention should be applied when the tensorial expression is expanded. The velocity tensor $\tilde{u}_i$ is of first rank and contains the velocities corresponding to the three spatial directions $x_i$, the scalar $\tilde{p}$ is the pressure and $\rho$ and $\nu$ are constants for the density and kinematic viscosity, respectively. When analyzing turbulent flows, it can be useful to decompose the velocities and the pressure into a mean part and a fluctuating part,

$$\tilde{u}_i = U_i + u_i, \tag{2.3}$$

$$\tilde{p} = P + p, \tag{2.4}$$

this is often called Reynolds decomposition. Here capital letter quantities are ensemble averages and lower-case letters represent fluctuations. Taking the ensemble average of equations 2.1 and 2.2 yields the following equations for the mean flow,

$$\frac{\partial U_i}{\partial t} + U_j \frac{\partial U_i}{\partial x_j} = -\frac{1}{\rho}\frac{\partial P}{\partial x_i} + \nu \frac{\partial^2 U_i}{\partial x_j \partial x_j} - \frac{\partial \overline{u_i u_j}}{\partial x_j} \tag{2.5}$$

$$\frac{\partial U_i}{\partial x_i} = 0. \tag{2.6}$$

These equations are called the Reynolds equations or Reynolds averaged Navier-Stokes (RANS) equations and are the equations that are most often solved in computations using turbulence models. Note the last term in equation 2.5, which is a derivative of the Reynolds stress tensor $-\rho\overline{u_i u_j}$. The overline is used to indicate ensemble averages. The Reynolds stress appears in the equations for the mean velocity as an unknown extra stress caused by the turbulent

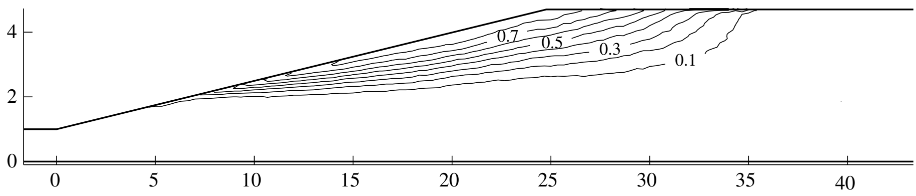

FIGURE 2.1. Backflow coefficient $\chi$ for the plane asymmetric diffuser flow.

fluctuations. The objective of single-point turbulence models is to model this term as accurately as possible. Modelling is needed since equations 2.5 and 2.6 only constitute four equations but the number of unknowns are ten (six unknowns in the Reynolds stress tensor due to index symmetry). This is called the closure problem of turbulence modelling.

## 2.2. Turbulent boundary layer separation

Boundary layer separation on a smooth surface occurs if the boundary layer is subjected to a strong enough adverse pressure gradient (APG) and if the duration of the APG is long enough. APG boundary layers grow more rapidly than for instance zero pressure gradient (ZPG) boundary layers since an APG is associated with a deceleration of the external flow and we get from the continuity equation (equation 2.6) that the wall normal velocity component $U_2$ will depend on the deceleration of the streamwise velocity as

$$U_2(x_1, x_2) = -\int_0^{x_2} \frac{\partial U_1}{\partial x_1} \mathrm{d}x_2, \tag{2.7}$$

in a two-dimensional flow where $U_3 = 0$. The boundary layer will hence grow not only due to momentum diffusion, as in the ZPG case. If the APG is sustained, the velocity in the near-wall region will continue to decelerate and eventually reverse and form a separated region. Turbulent boundary layers can sustain adverse pressure gradients longer than laminar ones due to the increased momentum diffusion caused by the turbulence that more efficiently brings down high-velocity fluid towards the wall.

Turbulent boundary layer separation is, in contrary to most laminar separations, a nonstationary phenomenon and the location of the point on the wall where backflow first occurs will fluctuate. The most common definition of the separation point is that it is the point where the mean wall shear-stress is zero but this measure does not tell us anything about where the instantaneous separation points are located. However, the backflow coefficient $\chi$, defined as the fraction of time that the flow is reversed does tell us something about the separation point movement. Figure 2.1 shows the backflow coefficient measured in the plane asymmetric diffuser, and it can be seen that there is no

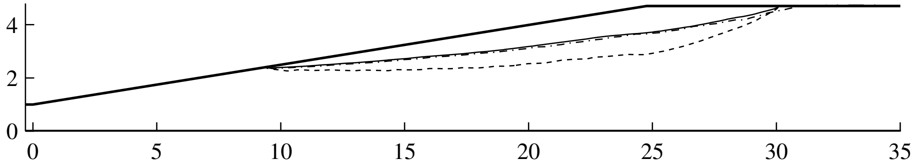

FIGURE 2.2. Comparison between different definitions of the separation bubble; dividing streamline (- - -), zero streamwise mean velocity (—) and backflow 50% of the time (– · –).

(or only a very small) region where there is backflow at all times. This is because the velocity fluctuations are of the same order or larger than the mean velocity. In Simpson *et al.* (1981) it is suggested that the backflow velocity is supplied intermittently by large-scale structures as they pass through the separated flow. Hence, the mean streamlines of a turbulent separated region may give the somewhat wrong impression that the backflow region is one large coherent recirculation zone.

The flow case investigated in this thesis cannot be directly compared to separating boundary layers with a free-stream as it is an interior flow in which the separated region is highly affected by the presence of the straight wall.

I have after studying many articles and several textbooks and questioning my colleagues, found that the term separation bubble have different meanings depending on who you ask. I have encountered three different definitions or interpretations for the limits of a separation bubble: (*i*) the separation bubble is the mean recirculating region within the dividing streamline (also called separation streamline) reaching between the stagnation points on the wall at the separation and reattachment points, (*ii*) the separation bubble is the region with mean backflow *i.e.* below the curve of zero mean velocity and (*iii*) the separation bubble is the region with backflow more than 50% of the time. The differences between these three definitions are illustrated in figure 2.2 which is based on the measurements presented in this thesis. Personally, I prefer the first definition which also seems to be the most established one in the literature.

In a recent paper Haller (2002) presents a kinematic theory for an unsteady laminar separation bubble, and it is shown that the instantaneous location of the point of zero wall shear-stress does not always coincide with the separation point, defined as the intersection between the wall and the separation profile (a material line that collects and ejects fluid particles from the vicinity of the wall). The separation profile is basically what one would see in a experimental visualization of the flow.

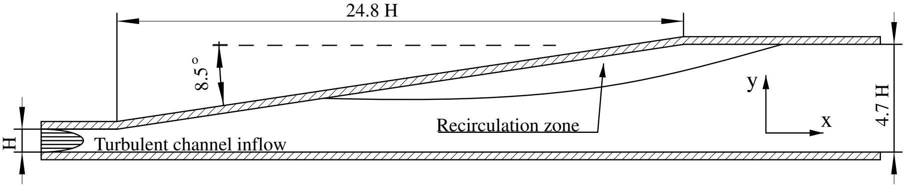

FIGURE 2.3. The plane asymmetric diffuser.

## 2.3. The plane asymmetric diffuser

The plane asymmetric diffuser used in the present experiment (see figure 2.3) is a generalized geometry for studies of two-dimensional duct flow separation, separation control and turbulence model testing. The inlet flow condition is fully developed turbulent channel flow, this makes it easy to match the experimental conditions in computations. The plane asymmetric diffuser, has prior to this study, been investigated in two independent experiments by Obi *et al.* and by Buice & Eaton. Results from these experiments have been published at several occasions in Obi *et al.* (1993*a*), Obi *et al.* (1993*b*), Obi *et al.* (1997), Buice & Eaton (1997) and Buice & Eaton (2000). Both studies concern diffusers with an opening angle of 10°. The experimental data from these experiments have been used for turbulence model evaluation in several studies, *e.g.* Obi *et al.* (1993*a*), Apsley & Leschziner (1999), Hellsten & Rautaheimo (1999), Gullman-Strand *et al.* (2002). These investigations did not concern so much the physics of the flow but were more concentrated on turbulence modelling aspects. Kaltenbach *et al.* (1999) made a computational investigation of the flow using large-eddy simulation which besides computational aspects also discusses the flow dynamics.

Unlike these previous investigations, this work concerns the flow in a diffuser with an opening angle of 8.5°. We chose to have a smaller angle in order to have a smaller separation and possibly have a better two-dimensionality of the flow. The smaller separation will also be more sensitive to the control methods which are to be tested in a later stage of this investigation. It is also more common to find flows on the verge of separation in practical applications.

CHAPTER 3

# Experiments

The experimental approach is, at present, the only alternative if one wants to investigate the turbulent plane asymmetric diffuser flow at reasonably high Reynolds numbers. We are still some years from being able to do a fully resolved direct numerical simulation (DNS) of this flow at the same Reynolds number as in this study.

## 3.1. Experimental facility

The experiments were performed in the specially designed closed loop wind-tunnel depicted in figure 3.1. A detailed description of the wind-tunnel design can be found in paper 3 in this thesis.

The approximately three meter long inlet channel has the purpose of producing the fully developed turbulent channel flow which is the inlet condition for the diffuser. The channel height being 30 mm means that the inlet channel is 100 heights long, which should be more than sufficient for a fully developed flow. Furthermore, the width of the inlet channel is more than 50 heights in order to reduce end-wall influences on the flow. Large parts of the measurement section are made in transparent materials to enable the use of optical measurement techniques (see sections 3.2.1 and 3.2.2). The flow after the diffuser is allowed to relax in a two meter long channel in order to reduce the influences from the downstream conditions on the diffuser flow. A circular pipe with 400 mm diameter leads the flow back to the fan inlet, this allows smoke to be used for flow seeding.

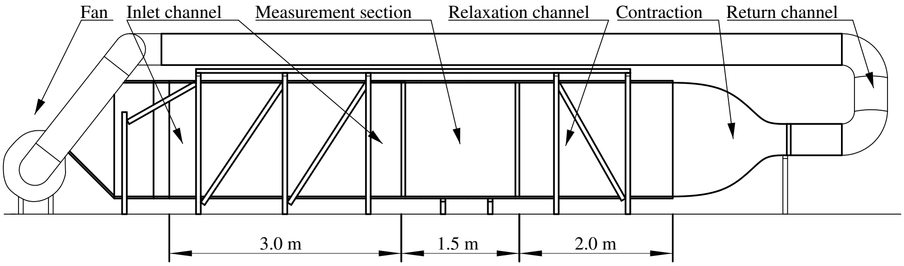

FIGURE 3.1. The wind-tunnel used for the experiments.

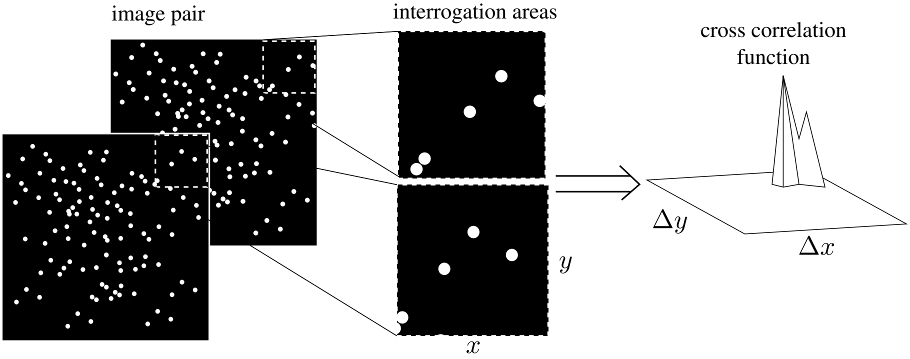

FIGURE 3.2. The PIV analysis procedure.

## 3.2. Measurement techniques

Besides particle image and laser doppler velocimetry, measurements of pressure differences have been performed in this study. A digital differential pressure transducer was used to measure the static pressure distribution through the diffuser and to monitor the wall shear-stress in the inlet channel using a Preston tube.

### 3.2.1. *Particle image velocimetry*

A major part of the measurements presented in the papers in this thesis were made using digital particle image velocimetry (PIV). The principle for PIV is rather straightforward, it is based on two photographic images of an illuminated plane in the fluid. If the fluid has been mixed with light reflecting particles (so called seeding particles) these will appear in the images as bright dots. The two images are taken within a time interval that is short enough to be able to see the same particles in both images, knowing the time between the images the velocity of the particles can be calculated from their displacement between the images. As light source for the illuminated plane it is common to use a pulsed laser, synchronized with the camera, which can deliver light at much higher intensities than other light sources, allowing short exposure times for sharp images. For example, the laser used for the measurements in this thesis has a maximum power of approximately 40 MW in each light pulse, although the duration of the pulse is only about 10 ns.

In digital PIV the images are taken with a digital camera. The digital images are divided into interrogation areas of $2^n \times 2^n$ pixels, the corresponding interrogation areas from the the image pair are cross-correlated in order to find the most probable displacement of the particles in each interrogation area.

Figure 3.2 gives a schematic view of this procedure. By choosing the interrogation areas to be $2^n \times 2^n$ pixels the two-dimensional fast Fourier transformation (FFT) algorithm can be utilized for finding the autocorrelation function, this decreases the computational effort needed for the image evaluation. The output from PIV is an instantaneous field of velocity vectors which gives direct information on the spatial structure of the flow. A disadvantage of the PIV technique is the often poor temporal resolution and the large amount of data that needs to be stored if many samples are taken in order to get reliable statistical averages. See section 2.2.2 in Paper 1 on page 27 for details on the PIV measurements in this particular study.

### 3.2.2. *Laser doppler velocimetry*

Laser doppler velocimetry (LDV) was used in this investigation to measure the velocity component perpendicular to the plane where the PIV measurements were taken. LDV is primarily based on two physical principles, the Doppler effect and the heterodyne principle. The Doppler effect is the phenomenon that an object moving towards a wave source will receive waves with another frequency than a stationary object would. For instance, if an object is moving towards the wave source (sending with the frequency $f$) with a velocity $v$, the object will receive waves with the frequency $f_{obj} = (c+v)/\lambda$, where $c$ is the propagation velocity of the wave and $\lambda$ is wavelength of the wave. The object will reflect waves with the shifted frequency $f_{obj}$, which will have a wavelength $\lambda_s = (c-v)/f_{obj}$ and frequency $f_s = c/\lambda_s$ when they are received by the sender. The difference in frequency between the waves sent out and received by the sender will be $\Delta f = f_s - f = 2cv/(\lambda(c-v)) \approx 2v/\lambda$ if the velocity of the object is small relative to the propagation velocity of the wave.

The heterodyne principle says that if two waves are superimposed, the amplitude of the resultant wave will vary at a frequency equal to the difference in frequency between the two superimposed waves. This is utilized in LDV by mixing the reflected wave with the wave that was originally sent out on the detector surface of a receiver. The receiver will hence measure a signal with an

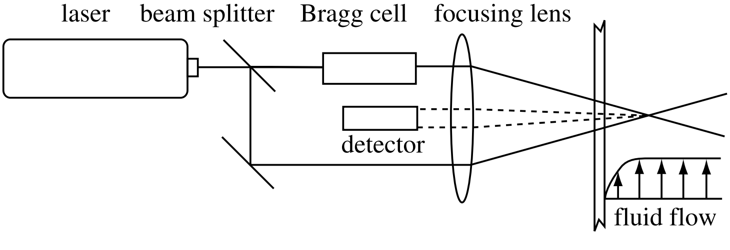

FIGURE 3.3. Sketch of a directional sensitive LDV setup in backscatter mode.

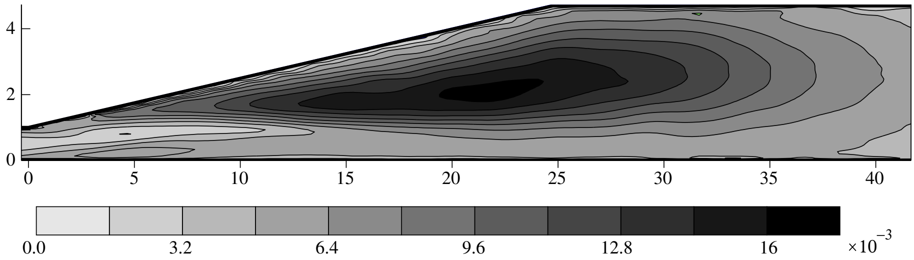

FIGURE 3.4. The turbulence kinetic energy $K/U_b^2$.

amplitude varying with the frequency $\Delta f$. Theoretically, it is not necessary to make use of the heterodyne principle in order to determine the velocity of the object but in practice it is very difficult to directly measure the frequency of the reflected light.

Figure 3.3 shows the principal setup for a directional sensitive LDV-system in backscatter mode, such as the one used in this study. Here, one has two laser beams coming in from two different directions, the scattered light from the upper beam in figure 3.3 will have a higher frequency than the incoming light and the light from the lower beam will be scattered with a lower frequency. The detector registers the difference in frequency between the two scattered beams as a varying light intensity each time a particle passes through the point of intersection between the two beams. The Bragg cell visible in figure 3.3 changes the frequency of one of the laser beams with a known constant shift (often with 40 MHz) to allow determination of the flow direction. If no Bragg cell is used, it is impossible to determine whether the flow is coming from the top of the figure or from below since the frequency difference between the reflected light from the upper and lower beams would be the same. See section 2.2.1 in Paper 1 on page 26 for details on the LDV measurements in this particular study.

## 3.3. Results

The measurements were made at a Reynolds number $Re_\tau = u_\tau H/\nu = 2000$, where $u_\tau$ is the friction velocity in the inlet channel and $H$ is the inlet channel height. All PIV and LDV measurements where taken in a plane near the centerline of the diffuser. The separation and reattachment points where found to be located at a distance of 9 and 31 inlet channel heights downstream of the diffuser inlet.

Figure 3.4 shows the turbulent kinetic energy $K = 0.5u_i^2$ of the diffuser flow, this quantity is composed of velocity measurements in all three spatial directions. Notice especially the high levels of turbulence kinetic energy that appear in the shear layer on top of the separated region and the tongue of low

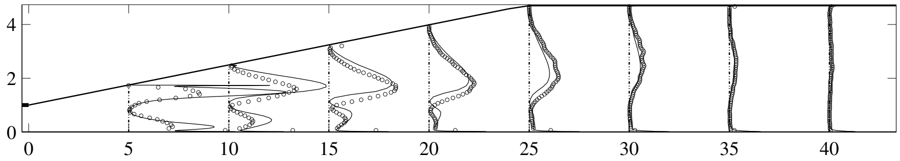

Figure 3.5. The production rate of turbulence kinetic energy $\mathcal{P}H/U_b^3 + x/H$. Comparison between measurements (○) and EARSM computation (—).

turbulence energy emerging from the inlet channel. The measured dataset has been used to evaluate a RANS computation using an explicit algebraic Reynolds stress turbulence model (EARSM). The computation was performed by Johan Gullman-Strand using the same code as in the computations presented in Gullman-Strand *et al.* (2002). The computational code is based on the finite element method and the governing equations are implemented through a symbolic computations interface using the femLego toolbox described in Amberg *et al.* (1999). The EARSM used is the one described in Wallin & Johansson (2000). In figure 3.5 the measured production rate of turbulence kinetic energy is compared to the results of the EARSM computation. It can be seen that the computation predicts higher production rates in the beginning of the diffuser and this overproduction is believed to result in an overestimation of the momentum diffusion towards the inclined wall leading to a delayed separation in the computations. In figure 3.6 the static pressure coefficient on the plane diffuser wall is shown and the smaller separation in the computation is perceptible as a higher pressure recovery and a less pronounced plateau region over the separation.

## 3.4. Control

One of the final goals of this study, which will continue for some more years after this thesis, is to develop techniques for separation control. So far only a preliminary test using vortex generators has been done. However, the vortex generator results were very positive. Figure 3.6 shows the pressure distribution through the diffuser for the case when a spanwise row of 20 mm high vortex generators were fitted on the inclined wall slightly above the location of mean flow separation. For comparison the pressure distribution for the case without vortex generators is included in the figure and the increase in pressure recovery when using vortex generators is quite substantial bearing in mind also that the vortex generators themselves cause flow losses.

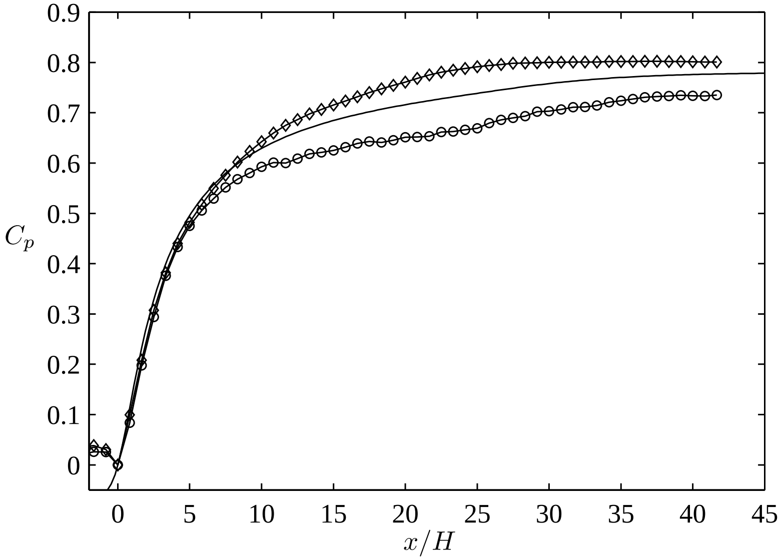

FIGURE 3.6. The pressure distribution through the diffuser for the uncontrolled flow (○), the flow with vortex generators (◇) and for a computation with an EARSM turbulence model (—).

CHAPTER 4

# Concluding remarks and outlook

The flow in a plane asymmetric diffuser with an 8.5° opening angle has been carefully investigated and a database which can be used for evaluation and improvements of turbulence models has been compiled. The flow case has been found to include several important and challenging phenomena, for instance streamline curvature effects around the diffuser's upstream corner, rapidly distorted turbulence in the beginning of the diffuser and pressure induced boundary layer separation and reattachment. A special wind-tunnel has been built for the experiment and tested with special attention paid to the two-dimensionality of the flow and to the long time mean velocity stability.

In the future the dataset will be complemented with near-wall measurements of the flow especially near the inlet corner of the diffuser where many phenomena important for the flow development are believed to occur. The streamline curvature correction described in Wallin & Johansson (2002) will be implemented and tested in new RANS computations. Another interesting thing to try, is to see if a differential Reynolds stress model (DRSM) satisfying strong realizability, such as the one of Sjögren & Johansson (2000), will be able to predict the near-wall asymptotics better than the DRSM:s tested in Apsley & Leschziner (1999). Rapidly distorted turbulence which is not in weak equilibrium is probably also handled better by a DRSM.

The control part of this project has yet merely been touched upon and more thorough work remains to be done here. The vortex generator test turned out to be a success and in the future similar approaches will be tested *i.e.* we believe that it is more efficient to control the separation by breaking up the spanwise homogeneity of the flow than only manipulating it in a two-dimensional fashion. Possible actuators that will be tested are inclined blowing jets, synthetic jets and plasma actuators. Computational studies of separation control might also be done using the forth order accurate finite difference DNS code described in Brüger (2002), and the large eddy simulation technique.

# Acknowledgment

First of all I would like to express my gratitude to my supervisor Professor Arne Johansson for giving me the possibility to be his student and for introducing me to the challenging field of turbulence research.

I also would like to thank my co-worker and office-mate Björn Lindgren for introducing me to the field of fluid mechanics experiments. Björn has besides being a good teacher also been a valuable friend.

I am very grateful to everyone at the department for contributing to a stimulating, enjoyable, friendly and relaxed atmosphere. I particularly appreciate the (sometimes lengthy) coffee breaks, not only for the coffee but also for the often interesting discussions. I have learnt a lot about all sorts of things during these breaks. Special thanks to all friends I have made at the department, with whom I have sailed, skied, travelled, played indoor bandy and football, barbecued, partied and much more.

The Swedish Energy Agency are gratefully acknowledged for their financial support.

# Bibliography

Amberg, G., Törnhardt, R. & Winkler, C. 1999 Finite elemet simulations using symbolic computing. *Mathematics and Computers in Simulation* **44**, 275–274.

Apsley, D. D. & Leschziner, M. A. 1999 Advanced turbulence modelling of separated flow in a diffuser. *Flow, Turbulence and Combustion* **63**, 81—112.

Brüger, A. 2002 Higher order methods suitable for direct numerical simulation of flows in complex geometries. *Tech. Rep.* 2002:07. Lic. thesis, Dept. of Mechanics, KTH, TRITA-MEK.

Buice, C. U. & Eaton, J. K. 1997 Experimental investigation of flow through an asymmetric plane diffuser. *Tech. Rep.*. Department of mechanical engineering, Stanford university.

Buice, C. U. & Eaton, J. K. 2000 Experimental investigation of flow through an asymmetric plane diffuser. *J. of Fluids Eng.* **122**, 433–435.

Gullman-Strand, J., Amberg, G. & Johansson, A. V. 2002 Study of separated flow in an asymmetric diffuser. In *Advances in Turbulence IX*, pp. 643–646. Southampton, U.K.

Haller, G. 2002 Kinematic theory of unsteady separation for two-dimensional flows. Under consideration for publication in J. Fluid Mech.

Hellsten, A. & Rautaheimo, P., ed. 1999 *Workshop on refined turbulence modelling*. ERCOFTAC/IAHR/COST.

Kaltenbach, H.-J., Fatica, M., Mittal, R., Lund, T. S. & Moin, P. 1999 Study of flow in a planar asymmetric diffuser using large-eddy simulation. *J. Fluid Mech.* **390**, 151–185.

Obi, S., Aoki, K. & Masuda, S. 1993*a* Experimental and computational study of turbulent separating flow in an asymmetric plane diffuser. In *Ninth Symp. on Turbulent Shear Flows*, p. 305. Kyoto, Japan.

Obi, S., Ishibashi, N. & Masuda, S. 1997 The mechanism of momentum transfer enhancement in periodically perturbed turbulent separated flow. In *2nd Int. Symp. on Turbulence, Heat and Mass Transfer, Delft, The Netherlands*, pp. 835–844.

Obi, S., Ohizumi, K., Aoki, K. & Masuda, S. 1993*b* *Turbulent separation control in a plane asymmetric diffuser by periodic perturbation*, pp. 633–642. Elsevier Science Publishers B.V.

Simpson, R. L., Chew, Y.-T. & Shivaprasad, B. G. 1981 The structure of a separating turbulent boundary layer. Part 2. Higher order turbulence results. *J. Fluid Mech.* **113**, 53–73.

Sjögren, T. & Johansson, A. V. 2000 Development and calibration of algebraic nonlinear models for terms in the Reynolds stress transport equations. *Phys. Fluids* **12** (6), 1554–1572.

Wallin, S. & Johansson, A. V. 2000 An explicit algebraic Reynolds stress modell for incompressible and compressible turbulent flows. *J. Fluid Mech.* **403**, 89–132.

Wallin, S. & Johansson, A. V. 2002 Modeling streamline curvature effects in explicit algebraic Reynolds stress turbulence models. *Int. J. of Heat and Fluid Flow.* **23**, 721–730.

# Paper 1

# Measurements in a plane asymmetric diffuser with 8.5° opening angle. Part I: General flow characteristics

**By Björn Lindgren, Olle Törnblom and Arne V. Johansson**

Dept. of Mechanics, KTH, SE-100 44 Stockholm, Sweden

To be submitted

The flow in an asymmetric plane diffuser with opening angle 8.5° has been studied in detail experimentally. The inlet condition was fully developed turbulent channel flow at a Reynolds number based on the inlet channel height and the friction velocity of $Re_\tau = 2000$. The mean and fluctuating velocities have been measured in all directions (streamwise, spanwise and wall-normal). A separated region is found on the inclined wall with a mean separation point at 9 and a mean reattachment point at 31 inlet channel heights downstream the diffuser inlet. Separation never occurs upstream of 5 inlet channel heights and reattachment never occurs downstream of 35 inlet channel heights. Two regions of special interest have been observed in the flow. A strong shear-layer between the separated region and the "outer" flow fluctuates substantially in wall-normal direction, interacting with the large scale vortices in the separated region. It is also influenced by the large adverse pressure-gradient and the rapid change in flow direction at the diffuser inlet corner on the inclined wall. The static wall pressure through the diffuser was measured and compared to a case where vortex generators are used to suppress the separation. The pressure coefficient was found to be almost 10% higher at the diffuser outlet for the case with vortex generators.

## 1. Introduction

Separation and the need for controlling the separation are essential in many applications of fluid flows. Particularly diffuser flows, *i.e.* duct flows subjected to a positive pressure gradient in the streamwise direction, are very common in many industrial applications. The aim of this study is to determine the characteristics of the separated plane asymmetric diffuser flow, to provide a reliable data-base for the turbulence modeling community and to identify flow mechanisms that can be used in future schemes for efficient separation control.

Many studies have been performed on geometry induced separated flow and adverse pressure gradient flows with separation. The backward facing step and the blunt plate have been investigated by *e.g.* Cherry *et al.* (1984), Eaton & Johnston (1981) and Kiya & Sasaki (1983). Ruderich & Fernholz (1975) performed an investigation on a normal bluff plate with a splitter plate using pulsed hot-wire anemometry. Some investigations closer to ours on turbulent boundary layer separated flow are reported by *e.g.* Perry & Fairlie (1975) Dianat & Castro (1991) and Angele (2002). There is also a review on the topic by Simpson (1989). Here, however we will concentrate on the plane asymmetric diffuser flow with fully developed turbulent channel flow as inlet condition.

The problem of computing the flow in this choice of geometry or to realize it experimentally are both very challenging tasks. The range of scales, the high turbulence intensities and the high strains encountered in this flow together with a large separated region makes it a demanding, and thereby well suited, problem for testing and developing turbulence models. The fairly simple geometry, for which a numerical conformal mapping for an orthogonal curvilinear grid can be derived, see *e.g.* Brüger (2002), simplifies the possibility to perform LES and DNS calculations in the future.

In the first part of our study, presented in this paper, we will concentrate on the mean flow characteristics of the flow in the diffuser and its nearby surroundings. The main reason is to provide good data of mean flow properties, such as mean and rms velocities, in the three spatial directions along the streamwise centerline of the diffuser where the flow is expected to be most two-dimensional. We will also investigate the extension of the separated region and look at measures such as the back-flow coefficient determining the features of the flow in the separated region.

In the second part of the study titled, *Measurements in a plane asymmetric diffuser with an opening angle of 8.5° opening angle. Part II: Turbulence characteristics*, we present properties especially interesting for turbulence modeling comparisons. We will look at characteristics of existing models and compare them to the behavior of the flow in the diffuser.

Flow in this geometry has previously been studied experimentally by *e.g.* Obi *et al.* (1993*a*), Obi *et al.* (1993*b*), Obi *et al.* (1997), Buice & Eaton (1997) and Buice & Eaton (2000). The opening angle of the diffuser was in all these studies slightly larger, 10°, than that (8.5°) used in the present work. The reason for choosing a smaller diffuser opening angle was here to reduce the size of the separated region, and thereby, in combination with a high aspect ratio of the diffuser, achieve a high degree of two-dimensionality of the flow and moderate unsteadiness of the separation and reattachment points. From a control study point of view a smaller separation bubble is desired to keep actuator amplitudes moderate. It is also more common to find flows at the verge of separation in practical applications, *e.g.* draft tubes, wind-tunnel diffusers, ventilation ducts etc.

Furthermore the intention of this study was to measure all necessary velocity components to be able to calculate the turbulent kinetic energy and to form the anisotropy tensor throughout the diffuser. These are very useful measures for the turbulence modeling community when new improved models are developed and evaluated. These data, mainly obtained from PIV images with a rather coarse grid, (each interrogation area is $4 \times 4$ mm$^2$), are to be complemented with measurements of velocity profiles with more data points to resolve the flow near the boundaries.

Among the above mentioned studies, Obi *et al.* (1993*a*) studied the plane asymmetric diffuser flow using a single component LDV. The measurements were then compared to calculations with two different turbulence models, (standard $k - \varepsilon$ and a basic version of SMC (second moment closure)). The agreement between the experimental data and the calculations were not very good although the SMC was better than the $k - \varepsilon$ model. They concluded that it is essential to capture the redistribution of energy between the different components, in this highly anisotropic flow, in the turbulence models.

Later Obi *et al.* (1993*b*) continued to study the same flow experimentally by inserting a periodic perturbation to the flow. The perturbation was generated by periodic blowing and suction through a slit in the spanwise direction. They investigated the influence of the perturbation frequency on the size of the separation bubble and found an optimum non-dimensional frequency, based on the inlet channel height and the inlet channel centerline velocity, around $St = 0.03$. They also concluded that at this perturbation frequency the enhancement of transport of momentum across the diffuser was maximized.

In Obi *et al.* (1997) they further investigated the effect of the perturbation on the production of the turbulent Reynolds shear stress separating the contributions from the perturbation and the mean flow. They found that at the optimum frequency the production of Reynolds shear stress and the interaction between the mean flow and the perturbation were both enhanced.

Buice & Eaton (1997), Buice & Eaton (2000) also made an experimental investigation in the same geometry (with 10°) increasing the diffuser aspect ratio and used primarily pulsed hot-wires to determine the flow in the separated region. Thermal tufts were used to find the separation and reattachment points. They also measured the wall shear-stress using pulsed wall-wire probes. Their results were used for comparison in a Large Eddy Simulation by Kaltenbach *et al.* (1999).

Brunet *et al.* (1997) made an experimental investigation on pressure effects on turbulent flow in a plane asymmetric diffuser with a smooth (10°) inclined wall. They compared their results to calculations using the $k - \varepsilon$ model and found that the model was particularly deficient in capturing the behavior of the Reynolds shear-stress.

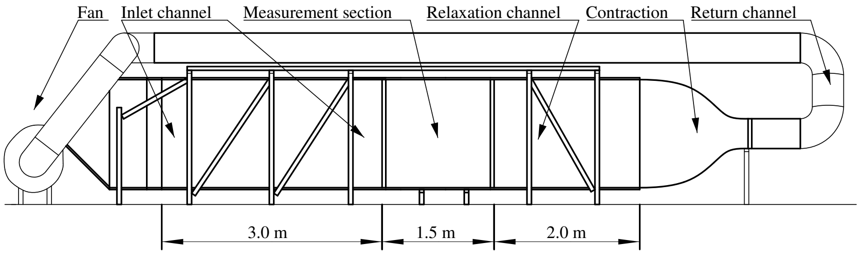

Figure 1. The wind-tunnel used in the experiments. The flow is circulating counter clockwise.

In the introduction to the second part of this paper there is a review of the numerous numerical and modeling efforts so far made using the plane asymmetric diffuser geometry. Some of these efforts have used the Obi *et al.* (1993*a*) and foremost the Buice & Eaton (1997) experimental data for comparison.

In future studies in the present set-up, control of the flow separation in the diffuser will also be investigated in co-operation with developers of control schemes. There have been a number of investigations involving control in various diffuser flow configurations, *e.g.* Coller *et al.* (2000); Obi *et al.* (1993*b*, 1997) but there is still much work to be done in this field.

## 2. Experimental setup

### 2.1. *Description of the wind-tunnel*

The experiments were performed in a closed loop wind-tunnel built specifically for this investigation. The wind-tunnel can be seen in figure 1. It consists of a blowing centrifugal fan delivering 11 kW of power followed by a section transforming the rectangular cross section shape of the blower outlet to another one with much higher aspect ratio. In this section splitter plates and screens ensure an even distribution of the fluid over the cross section area. The transformer is followed by a straight duct (settling chamber) which contains two screens at its upstream end to further even out mean flow variations. The settling chamber is followed by a two-dimensional contraction. The contraction further evens out mean flow variations and decreases the cross section height to 30 mm.

The contraction is followed by a turbulence generating grid and a 3.2 m long channel with a cross section area (width to height) of 1525 × 30 mm$^2$. The length to height ratio of the channel is thus larger than 100 ensuring fully developed channel flow at the outlet (see Comte-Bellot (1965)). This is important in order to obtain a well defined inlet condition to the diffuser which can also be easily produced in numerical calculations. At the downstream end of the inlet channel, the end walls (limiting the spanwise width of the channel)

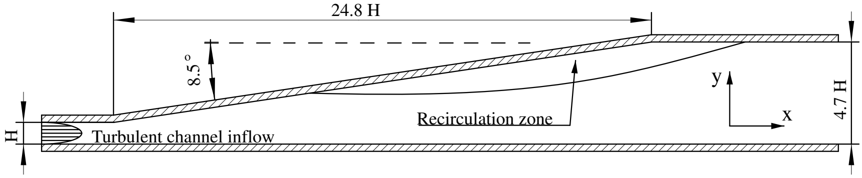

FIGURE 2. The measurement section of the wind-tunnel. A part of the inlet channel is seen to the left and part of the outlet channel is seen to the right. The view is from the top as referred to figure 1.

are perforated with 2 mm holes. This section is 100 mm long and the end wall boundary layers are removed through these holes by means of suction to prevent end wall boundary layer separation in the diffuser. Such a separation would destroy the two-dimensionality of the mean flow.

The inlet channel is followed by the diffuser. The diffuser has an inclined wall on one side and a straight wall on the other. The end walls are straight and equipped with three rows of vortex generators to further minimize the risk for boundary layer separation. The inclined wall has an angle of 8.5°, see figure 2. At the upstream corner of the inclined wall there is a radius of 100 mm to prevent separation at this corner. The inclined wall is made of an aluminum sandwich plate. Pressure taps are located along the centerline in the downstream direction at every 100 mm. These pressure taps were used to confirm that the pressure on both the straight and inclined walls were similar at all downstream measurement positions. The straight wall and the end walls are made of Plexiglas® to allow the use of optical measurement techniques such as LDV and PIV. The straight wall is also equipped with pressure taps along the centerline in the downstream direction at an interval of 25 mm. There are also pressure taps in the spanwise direction 100 mm upstream the diffuser inlet on each side at 100 mm interval. These pressure taps are used to check the two-dimensionality of the incoming flow. The high aspect ratio, 50 at the diffuser inlet, is crucial to achieve a high degree of spanwise uniformity.

The diffuser is followed by an outlet channel which is 141 mm high (4.7 inlet channel heights ($4.7H$)) and 2.5 m long. The purpose of this channel is to avoid upstream influence on the flow from devises located further downstream. This channel is partly made of Plexiglas® to facilitate measurements and partly of Plywood. Here, there are also two hatches giving access to the inside of the tunnel. Along the extent where it is made of Plexiglas® there are also pressure taps along the spanwise centerline with the same interval as in the diffuser.

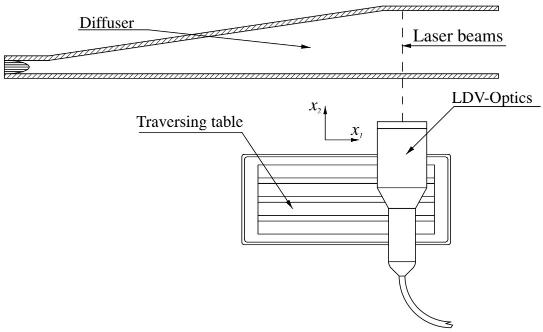

FIGURE 3. A sketch of the LDV measurement setup. The scattered light from the particles are received through the same optics as the emitted light.

The outlet channel is followed by a three-dimensional transformer changing the aspect ratio of the cross section area towards unity. The contraction is followed by a heat exchanger which is necessary in a closed return wind-tunnel to keep the temperature steady. A temperature sensor is located in the outlet channel and a computer logged the temperature which was found to be steady within ±0.5 °C. This is sufficient since the experiments performed here are not very temperature sensitive due to the fact that optical measurement techniques (LDV and PIV) are used instead of hot-wire anemometry.

Following the heat exchanger the cross section is converted from a rectangular to a circular shape. A pipe with 400 mm diameter then leads the flow back to the fan. At the end of the pipe the seeding particles (in this case smoke, see section 2.2.3) are injected into the flow. Just in front of the fan there is a slit ensuring atmospheric pressure at the fan inlet. This is important since it provides a constant reference pressure.

## 2.2. *Measurement techniques*

The measurement techniques used in this investigation were primarily Particle Image Velocimetry, PIV and Laser Doppler Velocimetry, LDV. Pressures were measured using a Furness Control FCO 510 differential pressure transducer with an accuracy of 0.25% of full scale (2000 Pa).

### 2.2.1. *LDV measurements*

The LDV is a one component FlowLite® system from Dantec. It has a He-Ne Laser of 10 mW emitting light with a wave length of 632.8 nm. The light beams have a Gaussian intensity distribution and the beam diameter was 3.23 mm between the beam expander and the focusing lens. The measurement volume

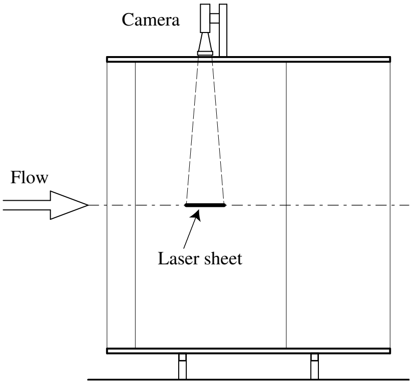

FIGURE 4. A sketch of the PIV measurement setup. The laser sheet is orientated horizontally, *i.e.* perpendicularly to the paper.

diameter using a lens with a focal length of 310 mm and a beam separation of 73 mm was 77 $\mu$m. The measurement volume length was 0.66 mm. In figure 3 a sketch of the LDV setup is shown. Note that the scattered frequency shifted light from the particles are received through the same optics as the emitted light, *i.e.* backscatter receiver technique.

The LDV was calibrated against a rotating wheel and used to measure flow components in the spanwise direction, *i.e.* $W$ and $w_{rms}$. The measurements of the spanwise component were made along the spanwise centerline of the diffuser at intervals of 50 mm. A total of 29 profiles were measured. In the wall normal direction, the interval varied with proximity to a wall and the downstream position, from 0.1 mm to 5 mm. These data were later also interpolated to give values on a common measurement grid. This grid have a spacing between points of 10 mm in the downstream direction and 2 mm in the wall normal direction.

Between 25000 and 100000 samples were taken at each measurement point for the ensemble average with the sampling rate varying between 200 and 1000 Hz. The time for collecting data was set to a minimum of 120 s at each point.

### 2.2.2. *PIV measurements*

In the streamwise and wall normal directions the velocity components were measured using a PIV system from Dantec. In figure 4 a sketch of the PIV setup is shown. The laser sheet is orientated horizontally and perpendicular to the paper in the sketch, and the camera takes images from above.

The system consists of a Spectra Physics 400 mJ double-pulse Nd-Yag laser, a megaplus ES1.0 digital double frame camera from Kodak and hardware processing and software from Dantec.

The infrared light emitted by the laser is doubled in frequency to obtain a visible light of 532 nm. CCD chips are most sensitive to light around this wave length. The duration of the pulses emitted by the laser is on the order of a few nano seconds. The light beam is guided from the laser through a Dantec flexible arm allowing changes in the light sheet position and orientation. A cylindrical lens at the end of the flexible arm converts the circular Gaussian beam into a light sheet with a thickness on the order of 1 mm. The intensity distribution of the light in the sheet is approximately Gaussian.

The CCD camera has a light sensitive chip of 1018 × 1008 pixels and an integrated memory chip allowing two images to be taken within 1 $\mu$s. The gray-scale resolution of the CCD chip is 256 levels. A f=60 mm lens was used together with a large aperture (f2.8) giving a very light sensitive image over an area of about the size of the outlet channel height in both directions.

The hardware, including all of the image processing, was supplied by Dantec. Through the hardware the camera and laser are synchronized. The image processing allowed for 32 double frame samples to be taken into each burst at a sampling rate of approximately 7.5 Hz depending on the maximum velocity in the image. Extra time for image processing was then needed to empty the memory containing the images before another burst could be recorded.

The software used to evaluate the images and calculate the velocity vectors was FlowManager 2.12 from Dantec. The software used sub-pixel interpolation to increase the velocity resolution assuming a Gaussian distribution. The datasets exported from the FlowManager software were, the velocity components, the streamwise and wall-normal position in the laser sheet plane, the peak ratio, *i.e.* the ratio between the two largest peaks in the cross correlation function between the two images, and an indicator, (0 or 1), indicating if the velocity vector was rejected according to the rejection criteria set in the software. A new evaluation with extended rejection criteria was later performed with Matlab based software.

The image size of the PIV was calibrated against a ruler that was inserted into the laser sheet before each measurement. Data was collected from 2048 images to form reliable mean and rms values. The size of the interrogation areas were $32\times32$ pixels. In physical space this is equivalent to approximately $4.5\times4.5$ mm$^2$. A 50% overlap between the interrogation areas were used throughout the measurements. In the inlet channel just upstream of the diffuser a more highly resolved image was used with another lens, (180 mm), to obtain more velocity vectors in this narrow channel. With the $1018\times1008$ pixel CCD chip, an interrogation area of $32\times32$ pixels and 50% overlap, the images contain $62\times62$ velocity vectors. Adding the fact that each interrogation area is $4.5\times4.5$

mm$^2$ the physical size of the images are 145 × 145 mm$^2$ which just covers the outlet channel height of 141 mm.

The time between frames was optimized for each set of pictures and varied with the downstream position. In general each measurement of 2048 frames took about 30 min to collect. To cover the entire measurement section PIV images were obtained at 11 downstream positions. A GUI Matlab script was used to match the streamwise and wall normal positions from the 11 sets of data.

These data were then, together with the LDV wall normal profiles of the spanwise velocity component interpolated on a common grid with a mesh size of 10 mm by 2 mm in the streamwise and wall-normal directions respectively. This grid is used whenever contour plots of the flow in the entire measurement section are shown in the section 3 of this paper.

### 2.2.3. *Seeding particles*

In both the PIV and LDV measurements the air was seeded with smoke from a smoke-generator ZR12-AL from Jem using a mixture of glycerol and water. By varying the amount of water the density of the smoke can be optimized to give good results. The smoke was inserted through the reference pressure slit just upstream of the fan and was sufficiently spread out in the measurement section due to the mixing in the fan and in the inlet channel. No attempt to measure the physical size of the seeding particles has been made but from previous investigation using the same type of smoke we can conclude that they typically are a few $\mu m$ in diameter.

### 2.2.4. *Error sources in LDV and PIV measurements*

It is very important to study the errors in the velocity measurements using the PIV and LDV techniques. Kristian Angele has investigated the error sources found in digital PIV (which is used here). His results will appear in a paper currently under preparation and the references here to his investigation is through private communication, Angele found that even carefully made measurements can have large errors but most of the errors can be eliminated by using appropriate validation criteria. PIV random error sources can *e.g.* be noise which can come from background disturbances, poor image contrast or resolution. Using a digital FFT to process the data will introduce small random uncertainties.

Another error source is the so called loss of pairs which means that a particle is only present in one of the images in an image pair. This is evidently more likely to happen for fast particles which gives a bias towards lower velocities. If the particle density is too low this problem will increase since the number of particles that form the correlation pair are fewer. This problem can be relieved by applying a weight function to the correlation plane, see *e.g.* Raffel *et al.* (1997).

A large velocity gradient over an interrogation area will not only cause the problem of integration but it will also decrease the signal to noise ratio. Following a criterion based on the velocity gradient, the time between images and interrogation area size in physical units and pixels introduced by Adrian & Keane (1992) makes sure this error source is kept small.

Finally peak-locking errors, *i.e.* the tendency of instantaneous particle displacements towards integer pixel values, is thoroughly investigated by Angele. An interrogation area is usually too small to give more than 8-16 possible discrete velocities. Therefore a curve-fit is applied in the correlation plane to get sub-pixel accuracy. This does not always eliminate the error which can be seen in the probability density distributions. Angele found that the limiting factor for peak-locking is that the ratio between the discretization velocity and the rms-velocity, *i.e.* the number of velocity peaks distributed over the probability density distribution. A symptom of peak-locking error is a shaky $u_{rms}$-profile. There are some symptoms of peak-locking problems in our measurements, see figure 7 as the mean velocity variation in our case is rather high.

LDV error sources may be reflections close to the wall decreasing the signal to noise ratio substantially and making it impossible to measure. Very close to a wall vibrations of the wall causes erroneous velocity peaks in the probability density distribution also largely affecting the measurements.

When measuring with an LDV system it is important to collect statistically independent samples *i.e* a single burst shall only be sampled once. It is also important to correct errors from high velocity bias, *i.e.* high velocity particles are more often detected than low velocity particles. The correction can be made by weighting the sample with its residence time, *i.e.* the time the particle are within the measurement volume. Arrival time averaging can be used to correct for low velocity bias at low data rates, see *e.g.* Fischer *et al.* (2001).

Averaging effects over the measurement volume while measuring in velocity gradients is an error source that can be quite substantial but it can be corrected for. Durst *et al.* (1998) derived an equations for correcting the mean and fluctuating velocity assuming elliptical shape of the measurement volume and that the scattering particles are mono-disperse.

Measuring at high mean velocity with limited fluctuating velocity can be difficult if the mixing and filter frequencies are limited in the LDV system. This is a result of the low resolution of the velocity probability density distribution which causes large errors in the measured fluctuating velocity. Our LDV system have these limitations and therefore we only used the LDV for the spanwise velocity component which has zero mean velocity. Many of the difficulties described above such as velocity gradient effects are therefore avoided.

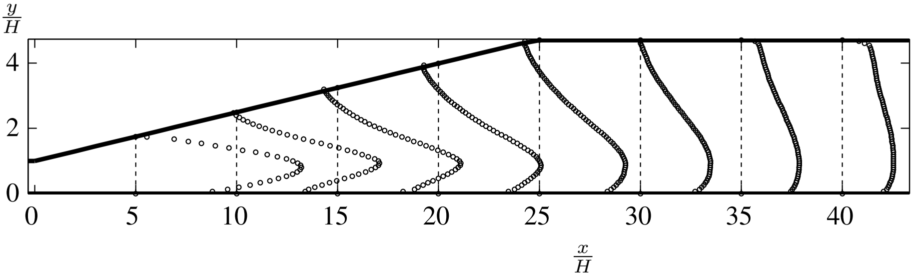

FIGURE 5. Streamwise mean velocity, $\left(U_{\text{fig}} = 10\frac{U}{U_b} + \frac{x}{H}\right)$, at 8 streamwise positions ($x/H = 5, 10, 15, 20, 25, 30, 35$ & 40). Dashed lines indicate zero level for each streamwise velocity profile.

## 3. Results

We here focus on the mean velocity components and fluctuation intensities. Results are also presented for the turbulence kinetic energy as well as for the stream function and back-flow coefficient, which both characterize the mean properties of the separated region at the inclined wall. Furthermore, the static wall-pressure along the spanwise centerline downstream through the diffuser is presented from which the pressure coefficient can be calculated.

### 3.1. *Velocity components*

In this study we measured all three velocity components and their fluctuations using PIV for the streamwise and wall-normal components and LDV for the spanwise component. Here, results for all these quantities are presented with the exception of the mean spanwise component which is zero within the measurement accuracy. The coordinate system is here defined as $x$ in the "streamwise" direction, $y$ in the "wall-normal" direction and $z$ in the spanwise direction. The corresponding average velocities are denoted respectively by $U$, $V$ and $W$. The y-component is of course only normal to the lower, straight wall but because of the relatively small opening angle, we prefer to here to refer to the x and y velocity components as streamwise and wall-normal. In all figures the spatial coordinates are normalized with the inlet channel height, $H = 0.03$ m, and the velocities are normalized with the inlet channel bulk velocity, $U_b = 20.0$ m/s, defined as

$$U_b = \frac{1}{H}\int_0^H U \mathrm{d}y. \tag{8}$$

### 3.1.1. *Streamwise mean and fluctuating velocities*

The diffuser can be divided into a region below the maximum velocity peak, *i.e.* close to the straight wall, and a region, above the velocity peak, including the separated flow region closer to the inclined wall, see figure 5. On the side close to the inclined wall an inflection point is created almost immediately downstream the inlet in the streamwise velocity profile. The inflectional profile is enhanced downstream in the diffuser until the inclined part of the wall ends. Thereafter it relaxes towards the same profile as on the straight wall although at the maximum downstream position in this study the complete streamwise velocity profile is far from symmetric. The peak in streamwise velocity diverges slightly towards the centerline of the diffuser as it decreases in strength, but this process is very slow and still at our most downstream measurement position the streamwise velocity maximum is much closer to the straight wall than the inclined wall.

The inflection streamwise velocity profile creates a strong shear-layer which is important as it distributes momentum from the outer flow towards the separated region. The non-zero components in the Reynolds stress tensor, ($-u_{rms}^2$, $-v_{rms}^2$, $-w_{rms}^2$ and $-\overline{uv}$) all have their peaks within this shear-layer.

The very high fluctuation level of this flow with instantaneous velocity profiles very far from the mean value is illustrated in figure 6 through a sequence of instantaneous velocity fields in the streamwise, wall-normal plane. We can observe very large velocity variations which are of large scale in this region which includes the first (upstream) part of the separated region. High speed fluid (shown in white) emerging from the inlet channel is deflected towards the inclined wall directly downstream the inlet, but occasionally, an almost jet like character (figure 6q) can be observed with a resulting large separation region. This motion can, with a larger opening angle, lead to instantaneous separation along the straight wall. As will be shown later this is not the case here and we can conclude that the 8.5° opening angle is small enough to also avoid straight wall separation.

The motion of this high velocity region is of course intimately linked to the shedding process in the separated region. Unfortunately the sampling frequency of the measurement system is too low to be able to detect the shedding process. A sampling frequency 10 times higher than the 7.5 Hz available with our PIV system should be enough to resolve this process that is expected (loosely from Obi *et al.* (1993*b*) and Kaltenbach *et al.* (1999)) to have a mean frequency of about 20 Hz although a large variation in frequency is expected from these earlier studies and also judged from our instantaneous velocity images.

The fluctuating streamwise velocity is in general very large in this flow as was shown above in the instantaneous velocity fields. The fully developed turbulent inlet flow generates a $u_{rms}$ distribution which is symmetric and with

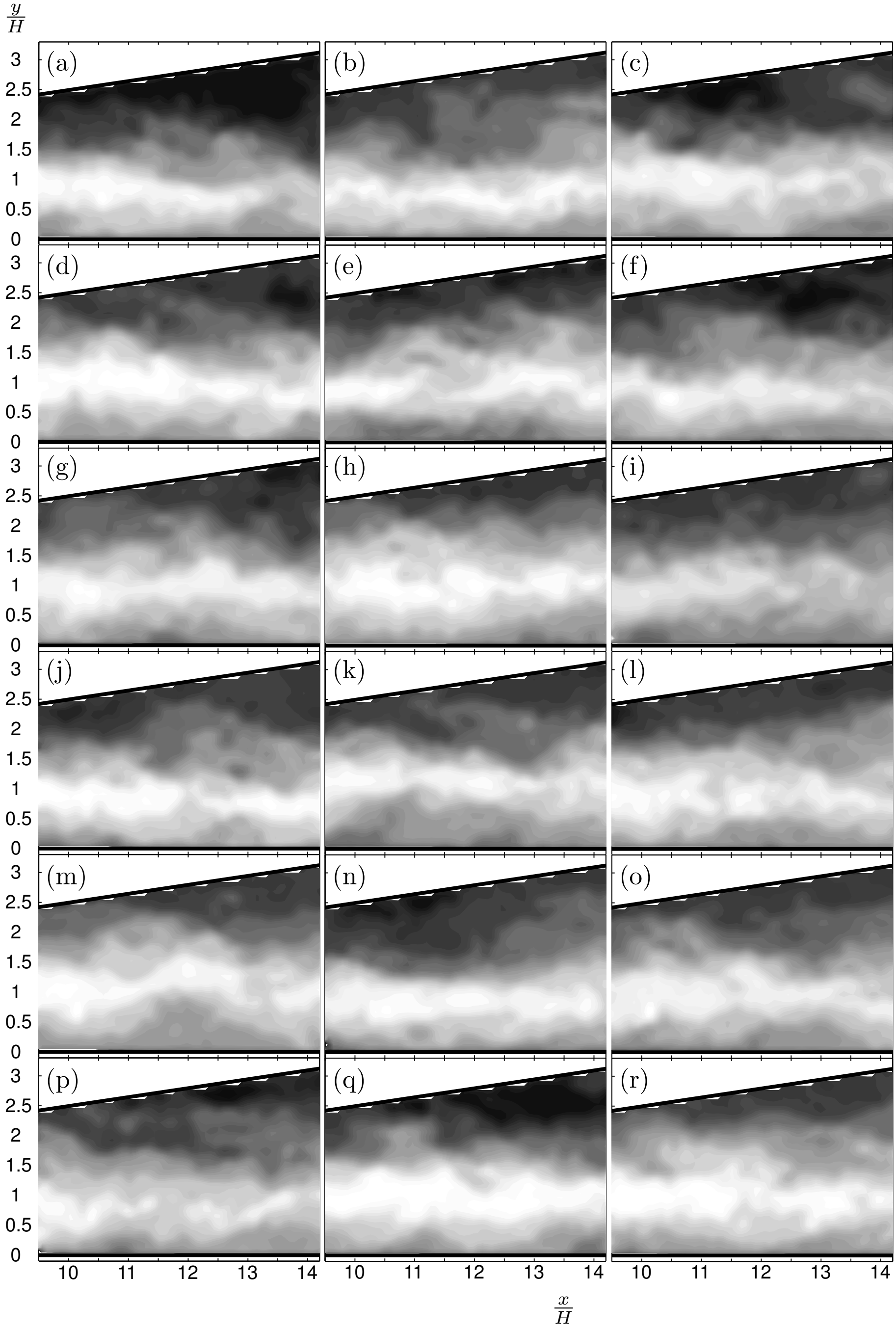

FIGURE 6. Time sequence of instantaneous velocity fields (U-V plane). $\Delta t = \frac{2}{15}$s between images. White: High positive velocity fluid (17 m/s). Black: Negative velocity fluid (-1 m/s).

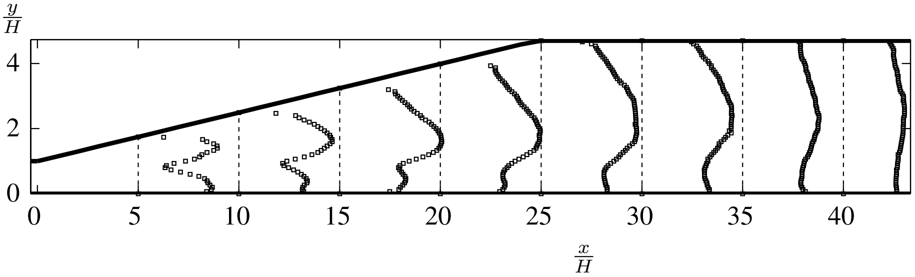

Figure 7. Root mean square of streamwise fluctuating velocity, $\left(u_{rms,\mathrm{fig}} = 40\frac{u_{rms}}{U_b} + \frac{x}{H}\right)$, at 8 streamwise positions ($x/H = 5, 10, 15, 20, 25, 30, 35$ & $40$).

peaks close to each wall and a local minimum at the centerline where the streamwise velocity gradient is zero. The development of these two peaks are rather different as the flow propagates downstream through the diffuser. The peak close to the straight wall is first slightly reduced downstream and eventually it is almost overtaken by the growing local maximum emerging from the upper part of the inlet channel. This peak grows and reaches its maximum at about $x/H = 20 - 25$, see figure 7. The location of this peak detaches from the inclined wall and follows the strong shear-layer outside the separated region. Eventually the fluctuating streamwise velocity reaches a symmetric distribution across the outlet channel with small variations along the profile. Thereby a distribution with two peaks at the inlet develops towards a distribution with one peak at the centerline. As the flow in the outlet channel is developing, the turbulent channel flow distribution will eventually be recovered far downstream.

### 3.1.2. *Wall-normal mean and fluctuating velocities*

The wall-normal velocity, $V$ (*i.e.* normal to the straight wall, and almost normal to the inclined wall) is very small in most parts of the diffuser. Close to the corner at the diffuser inlet where there is a rather abrupt change in the direction of the wall causes the flow to turn leading to locally high values of the wall-normal velocity (Not shown in figure 8). Further studies of this region is required with a better spatial resolution.

The wall-normal velocity decreases downstream (until about $x/H = 15 - 20$) where its peak slowly starts to grow again due to the decreasing height of the separation bubble. The location of this peak follows the strong shear-layer outside the separated region, see figure 8. The maximum value is found close to the centerline of the diffuser and the magnitude of the maximum increases up to approximately $x/H = 30$. Further downstream the peak follows the centerline of the outflow channel while decreasing in magnitude. The presence

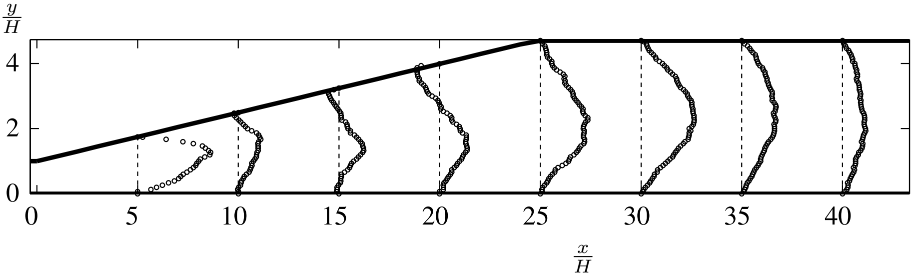

FIGURE 8. Wall-normal mean velocity, $\left(V_{\text{fig}} = 100\frac{V}{U_b} + \frac{x}{H}\right)$, at 8 streamwise positions ($x/H = 5, 10, 15, 20, 25, 30, 35$ & $40$). Dashed lines indicate zero velocity for each streamwise velocity profile.

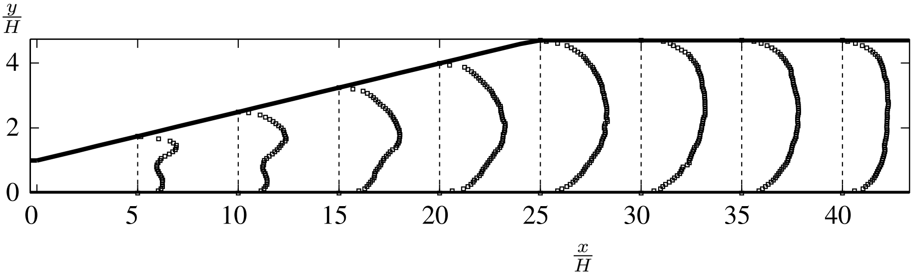

FIGURE 9. Root mean square of wall-normal fluctuating velocity, $\left(v_{rms,\text{fig}} = 40\frac{v_{rms}}{U_b} + \frac{x}{H}\right)$, at 8 streamwise positions ($x/H = 5, 10, 15, 20, 25, 30, 35$ & $40$).

of a vertical velocity in the core region of the outflow channel is of course due the asymmetry of the streamwise velocity component.

The fluctuating wall-normal, $v_{rms}$, velocity behaves much like the streamwise fluctuating velocity with peaks on either side of the centerline in the inlet channel and with a growth of the peak closest to the inclined wall and a reduction of the other peak. The variation of the wall-normal fluctuating velocity is however substantially smaller than for its streamwise counterpart and it reaches a symmetric profile at quite an early stage with a maximum at the outlet channel centerline. The maximum is reached at a downstream position approximately equal to the point where the inclined part of the wall ends as is also the case for the wall-normal mean velocity.

### 3.1.3. *Spanwise fluctuations, Reynolds stress and turbulence kinetic energy*

The development of the fluctuating spanwise velocity, $w_{rms}$, downstream through the diffuser resembles very much its streamwise counterpart. The main

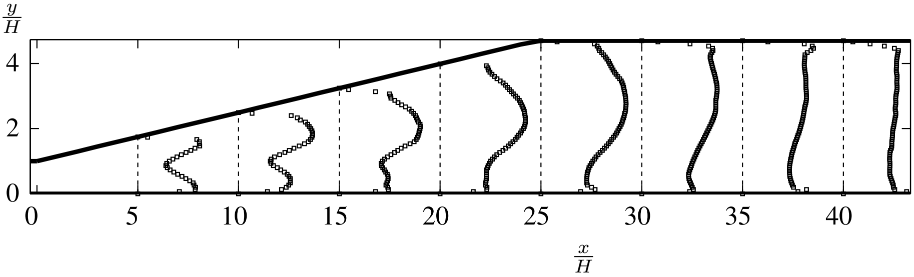

FIGURE 10. Root mean square of spanwise fluctuating velocity, $\left(w_{rms,\text{fig}} = 40\frac{w_{rms}}{U_b} + \frac{x}{H}\right)$, at 8 streamwise positions ($x/H = 5, 10, 15, 20, 25, 30, 35$ & $40$).

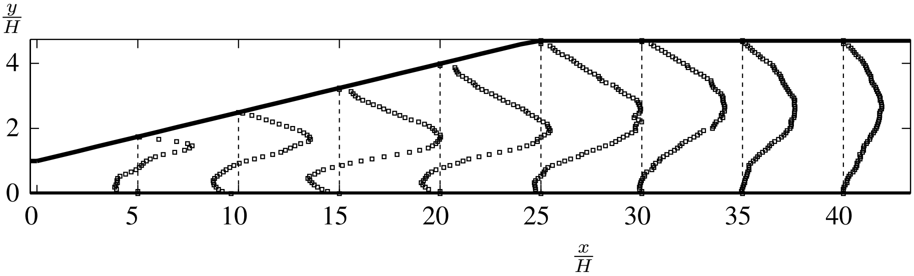

FIGURE 11. Reynolds stress in the streamwise wall-normal plane, $\left(\overline{uv}_{\text{fig}} = 1000\frac{\overline{uv}}{U_b^2} + \frac{x}{H}\right)$, at 8 streamwise positions ($x/H = 5, 10, 15, 20, 25, 30, 35$ & $40$).

difference lies in the smaller magnitude of the spanwise component. The wall-normal location of the maximum is also slightly different, with the maximum for the spanwise fluctuating velocity closer to the inclined wall, but still within the shear-layer outside the separated region. The maximum in streamwise direction is found at $x/H = 20 - 25$ which is similar to that for $u_{rms}$.

If the spanwise component cannot be measured in an experiment, it seems possible to obtain a first order estimate by rescaling of the streamwise fluctuating velocity. The main reason for making such an estimate would be to be able to estimate the turbulence kinetic energy without having to measure all three velocity components. This has been done in other studies, however, it is of course more appropriate to directly measure all components to get a correct value for the turbulence kinetic energy that can be used in comparison with results from *e.g.* turbulence model predictions.

The Reynolds shear-stress is a very important quantity since it redistributes momentum from high velocity regions to low velocity regions. A high level of Reynolds shear-stress is thus instrumental in suppressing separation, see *e.g.*

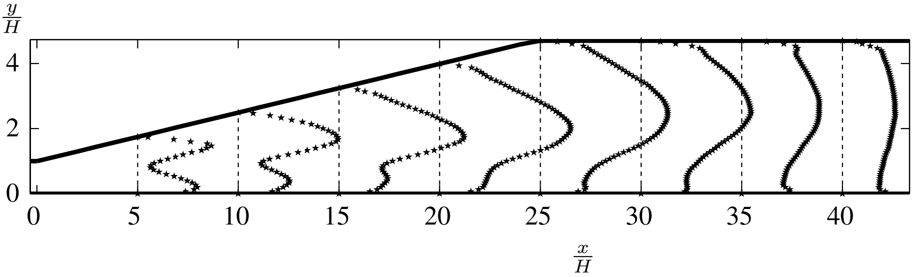

FIGURE 12. Turbulence kinetic energy, $\left(K_{\text{fig}} = 400\frac{K}{U_b^2} + \frac{x}{H}\right)$, at 8 streamwise positions ($x/H = 5, 10, 15, 20, 25, 30, 35$ & $40$).

Obi *et al.* (1993*b*). The amount of Reynolds shear-stress scales with turbulence kinetic energy which makes a flow like this, with fully developed turbulent channel flow as inlet condition, quite capable of handling a strong adverse pressure gradient and thereby reduce the size of the separated region.

The Reynolds shear-stress in the streamwise wall-normal plane, $\overline{uv}$, is antisymmetric in the inlet channel. With this coordinate system the negative peak is near the straight wall and the positive peak closer to the inclined wall. As the flow develops downstream in the diffuser the positive peak grows while the negative peak is suppressed, see figure 11. The maximum Reynolds shear-stress is found at $x/H = 20 - 25$ and thereafter it decreases in magnitude. The location of the positive peak follows the location of maximum shear in the shear-layer outside the separated region. At the end of the measurement region the Reynolds shear-stress attains a symmetric profile with the maximum located near the outflow channel centerline.

The turbulence kinetic energy, $K$, is a primary quantity for comparisons with turbulence model predictions since most models rely on transport equations for this quantity where one or more terms have to be modeled. Comparisons with numerical results can be improved if direct and accurate measurements of the turbulence kinetic energy are made. New insights that can assist in the development of new turbulence models can thereby be obtained. The dissipation rate, $\varepsilon$, can here however not be measured directly although some attempts using the PIV technique have been made *e.g.* by Baldi *et al.* (2002). The dissipation rate is needed for a complete comparison with turbulence models where it is included, directly or in some other form ($\omega$, $\tau$), through a transport equation.

In figure 12 the turbulence kinetic energy at eight streamwise positions is plotted. It is for natural reasons, similar in character to the individual intensities shown in previous figures. It is defined as

$$K = \frac{1}{2}\left(u_{rms}^2 + v_{rms}^2 + w_{rms}^2\right). \tag{9}$$

The maximum value is located at about $x/H = 20 - 25$ in the shear-layer outside the separated region as for the individual fluctuating components. The kinetic energy profile does not quite reach a truly uniform shape at our most downstream position.

It should be noticed that our measurements are not resolving the very near wall regions. Therefore our conclusions are excluding phenomena occurring in the immediate vicinity of the walls. In the future these measurements will be complemented by new experiments covering the near wall regions as well as a more detailed investigation of the upstream corner on the inclined wall where the expanding part of the diffuser begins. There we expect to find locally high levels of turbulence intensity and anisotropy as well as a strong streamline curvature. Some clues to these statements can be seen if the whole velocity field is studied rather than the isolated velocity profiles presented here.

### 3.2. *Characterization of the separated region*

To further study the separated region, extending the information gained by looking at the velocity profiles the stream-function, generating streamlines and the back-flow coefficient are useful tools. The back-flow is also studied through a sequence of instantaneous images.

#### 3.2.1. *Stream-function*

The stream-function is here defined as

$$\Psi(x,y) = 1 - \frac{1}{HU_b}\int_0^y U(x,y)\mathrm{d}y. \tag{10}$$

In figure 13, constant values of the stream function (streamlines) are plotted throughout the measurement region. This definition of the stream function gives a value of $\Psi = 0$ at the dividing streamline. The dividing streamline separates the (averaged) recirculation zone from the outer flow. The two positions where the dividing streamline reaches the "upper" wall are the mean separation and reattachment points, respectively. From figure 13, the mean separation point is found to be located at 9 channel heights downstream the diffuser inlet ($x/H \approx 9$) and the mean reattachment point is located at $x/H \approx 31$.

In figure 13 the gray-scale levels represent a measure of the speed in the diffuser, *i.e.* here $\sqrt{U^2 + V^2}$, with an increment of 2 m/s. The figure shows how the flow with maximum velocity first is deflected at the inlet corner towards the inclined wall but when it approaches the separation point it is deflected back towards the straight wall. Thereafter, there is a very slow relocation of the maximum towards the center of the outlet channel. It can also be noted that the decrease in speed is slower through the diffuser compared to an attached flow case. This follows from the constriction caused by the separated region, which decreases the adverse pressure gradient and slows down the retardation of the flow speed and spreads it out over a larger downstream length.

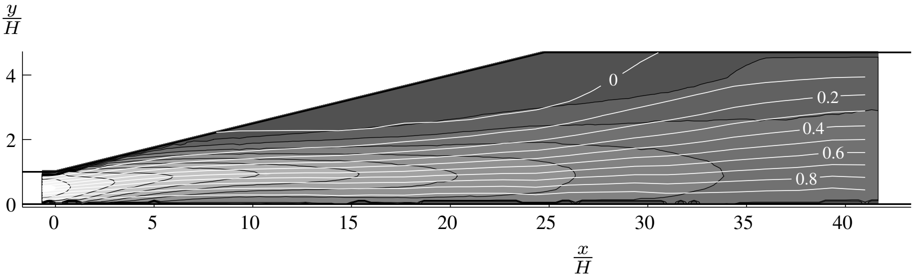

FIGURE 13. Streamlines shown as white curves. The stream function is integrated from the inclined wall. Gray-scale background with separating black curves shows the speed, with a contour increment of 2 m/s.

### 3.2.2. *Back-flow coefficient*

A very interesting quantity is the back-flow coefficient which relates the number of samples with negative velocity (along the inclined wall) to the samples with positive velocity. A back-flow coefficient of 1 means that all samples have negative velocity and a back-flow coefficient of zero thus means that all samples have positive velocity. The back-flow coefficient then reads

$$\chi(x,y) = \frac{1}{N}\sum_{k=1}^{N} \frac{1 - \mathrm{sgn}(u_k(x,y)\cos(\alpha) + v_k(x,y)\sin(\alpha))}{2}, \qquad (11)$$

where $N$ is the total number of samples, sgn is the sign function, $u_k$ the streamwise velocity in the $k^{\mathrm{th}}$ sample, $v_k$ the wall-normal velocity in the $k^{\mathrm{th}}$ sample and $\alpha = 8.5°$ the diffuser opening angle.

First, we notice in figure 14 that along the straight wall there seems to be no samples with back-flow although the rather poor resolution might allow for a very thin separation bubble very close to the wall. It is important that there is no separation on the straight wall since this may destroy the "stability" of the separation bubble on the inclined wall with a separation altering side from the inclined wall to the straight wall back and forth. Our choice of opening angle, 8.5° is thus small enough to avoid this kind of flow state.

Focusing our attention on the separation bubble on the inclined wall the back-flow coefficient gives us the streamwise locations on the inclined wall for the most upstream instantaneous separation point that in figure 14 is shown to be $x/H \approx 5$. The flow is separated 80% of the time downstream $x/H \approx 14$. In real time the separation point moves back and forth along the inclined wall and at some occasions the flow is completely attached. A back-flow coefficient of 0.5 gives the mean separation point, already shown to be $x/H \approx 9$ from the dividing streamline, and the mean reattachment point at $x/H \approx 31$. The

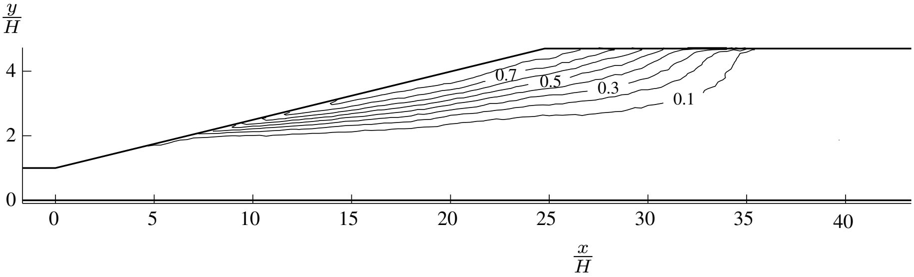

FIGURE 14. back-flow coefficient, $\chi$.

reattachment point never moves downstream of $x/H \approx 35$ where the flow thus always is attached.

To study the separation more in detail in time, figure 15 shows the instantaneous back-flow in a sequence of images. Black is large negative velocity along the inclined wall and white is positive velocity. It is clear from this sequence that sometimes the flow is almost fully attached (*e.g.* 15i and 15m) and sometimes there are large regions of flow with negative velocity. The formation of spanwise vortices can be seen in some of the frames in the time sequence of figure 15.

### 3.3. *Static wall-pressure distribution*

The static wall-pressure has been measured along the spanwise centerline in the downstream direction. Measurements on both the inclined and straight walls were performed but with a much better spatial resolution on the straight wall. The measurements on the inclined wall were made to confirm that the static pressure is constant in the wall-normal direction (within our measurement accuracy) through the diffuser. This is true for most of the downstream measurement positions except at the upstream corner where the rapid change in wall direction leads to large curvature of the streamlines and consequently pressure differences between the two sides.

Shown in figure 16 is the pressure coefficient, $C_p$, defined as

$$C_p(x) = \frac{p_w(x) - p_w(x=0)}{\frac{1}{2}\rho U_b^2}, \tag{12}$$

where $p_w$ is the static wall-pressure and $\rho$ the density of the air is shown. The diamonds in figure 16 represent the pressure coefficient with undisturbed flow. The start of the separation can be seen where the diamonds deviate from the circles. The following rather flat region is caused by the constriction to the outer flow produced by the separated region that decreases the pressure gradient.

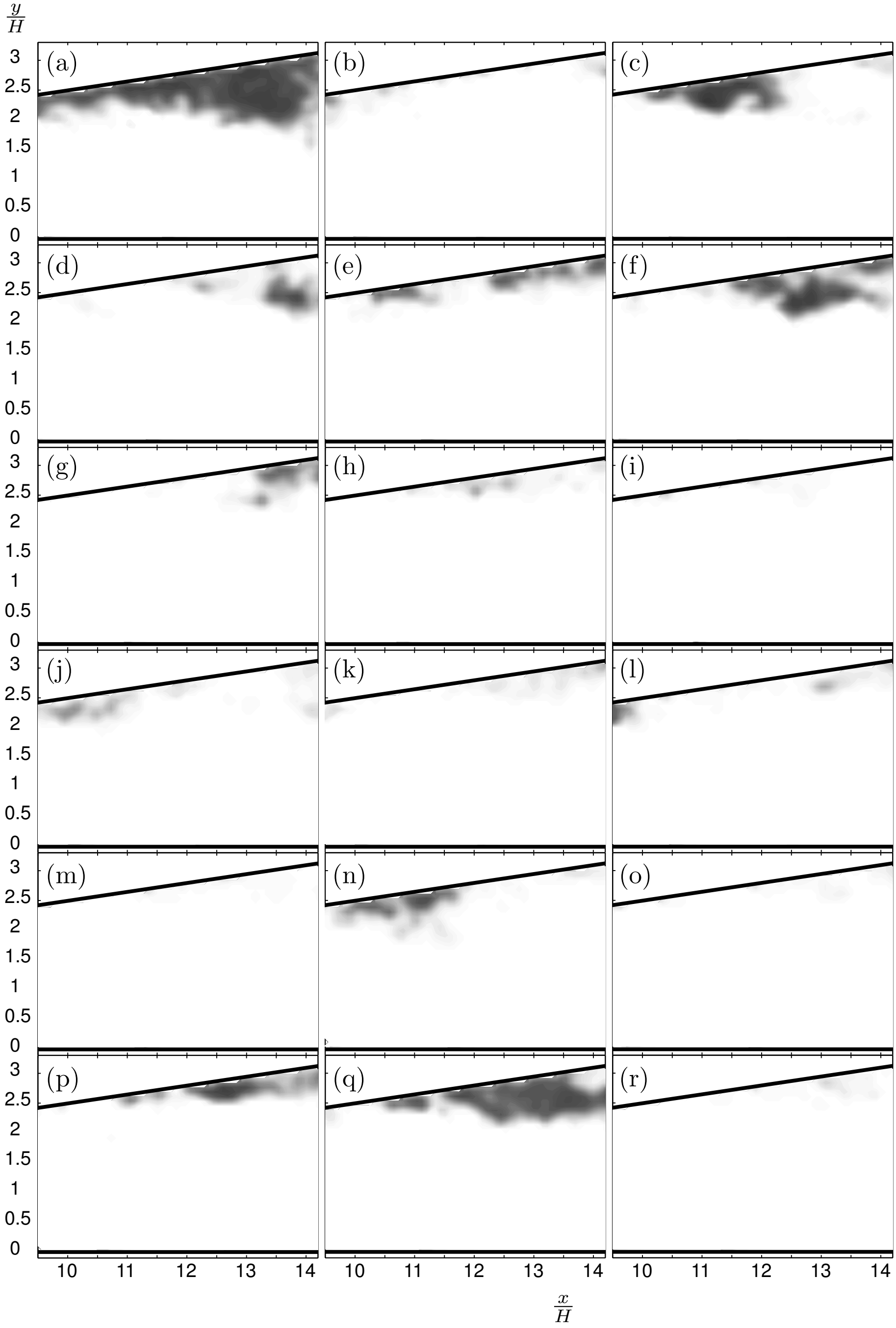

FIGURE 15. Time sequence of images of instantaneous negative streamwise velocity (x-y plane). $\Delta t = \frac{2}{15}$s between images. White: Zero or positive streamwise velocity. Black: Strong streamwise negative velocity.

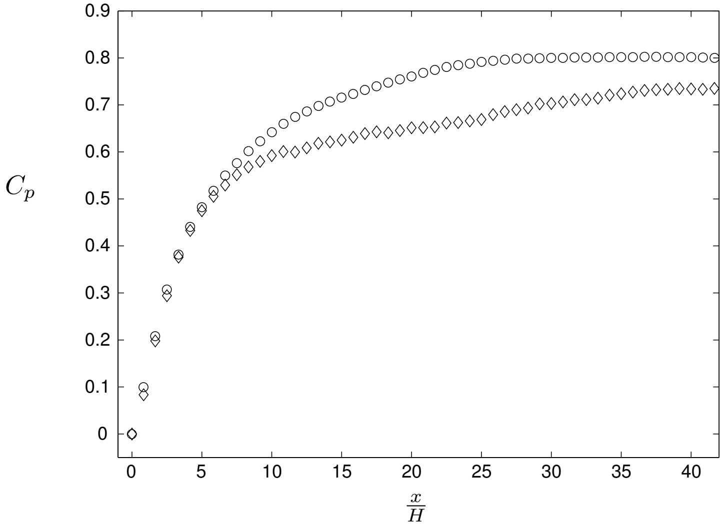

FIGURE 16. Static wall-pressure coefficient, $C_p$. Diamonds represent flow without vortex generators. Circles represent flow with vortex generators.

The circles represent a reference case where vortex generators have been installed to suppress the separated region. These vortex generators are positioned in a spanwise row at a downstream location of about $x/H = 7$. Their height is 20 mm and the angle of the vertical plates to the mean flow is 20°. The spanwise spacing between the vortex generators is 100 mm which gives a total of 15 generators covering the entire span of the diffuser. As can be seen in figure 16 the pressure coefficient continues to rise where the flat region, indicating separation in the uncontrolled case (diamonds), starts. The final pressure recovery increases with vortex generators from approximately 0.73 to 0.80 despite the extra pressure loss generated by the vortex generators themselves through the streamwise vortices they create.

## 4. Concluding remarks

The flow in an asymmetric plane diffuser has been studied with extra attention paid to ensuring good two-dimensionality of the mean flow. The focus in this paper is on the overall flow characteristics, *i.e.* mean velocities, turbulence intensities and Reynolds stresses, together with an investigation of the separated region using instantaneous velocity fields, streamlines and the back flow coefficient.

The streamwise mean velocity, $U$, gives us indications of where in the diffuser flow the most interesting flow features can be found. These are apart from the separated region at the inclined wall the strong shear-layer outside the separated region and the region just downstream of the diffuser inlet. Studies of instantaneous velocity fields reveal that a region of high velocity fluid emerges from the inlet channel, that gives almost a "jet-like" structure to the flow with large amplitude and large scale coherence of the fluctuating field, interacting with the large scale structures in the separated region. There is a certain risk for a small separation on the straight wall when the flow is attached along the inclined ditto but the rather moderate opening angle used here (8.5°) does not produce large enough gradients for this to happen. The inflectional streamwise velocity profile found around the edge of the separated region creates a strong shear-layer that is important as it distributes energy from the outer flow towards the separated region. The non-zero components in the Reynolds stress tensor, ($-u_{rms}^2$, $-v_{rms}^2$, $-w_{rms}^2$ and $-\overline{uv}$) all have their peaks in this shear-layer.

The wall-normal velocity, $V$, is very small in most parts of the diffuser, but close to the upstream corner at the diffuser inlet where the change in the direction of the wall is rather abrupt, locally high values of the wall-normal velocity and high streamline curvature are found. This region is not studied in detail in this paper since a better spatial resolution in the measurements is required.

The streamwise fluctuating velocity, $u_{rms}$, increases in magnitude downstream in the diffuser and peaks between $x/H = 20 - 25$. The typical, $u_{rms}$, two peak profile in the inlet channel flow is redistributed towards a one peak profile with the peak following the shear-layer outside the separated region and eventually its location in the outflow channel is close to the centerline. The other two components of the fluctuating velocity, $v_{rms}$ and $w_{rms}$, are subjected to the same transformation as the streamwise component, although the magnitude is smaller with $v_{rms}$ (about half the size of $u_{rms}$) and the magnitude of $w_{rms}$ lies in between $v_{rms}$ and $u_{rms}$. The location of the peaks in wall-normal direction is also somewhat different from the streamwise case.

The Reynolds shear-stress, $-\overline{uv}$, in the streamwise wall-normal plane is large in the shear-layer outside the separated region. Since the Reynolds shear-stress contributes to a redistribution of momentum toward regions with lower mean velocity it helps to delay the separation in the diffuser. The turbulent inlet channel flow contains a fair amount of turbulent kinetic energy which makes this diffuser flow more resistant to separation than if a laminar flow would have been chosen as the inlet condition.

The flow detaches on the inclined wall at approximately 9 inlet channel heights downstream from the diffuser inlet. The separation point moves, in time, up and down along the inclined wall but never above $x/H = 5$ as shown by the back flow coefficient figure. This movement is coupled to the shedding process in the separating region. The reattachment point is of course also moving in its location with the furthest downstream location of 35 inlet channel heights. The mean reattachment point was found to be at $x/H = 31$. By studying the instantaneous images of back flow in the separated region we get a fairly good view of the vortices created and swept downstream through the diffuser although the sampling rate of our PIV system is too low to be able to determine a mean ”shedding” frequency. Using other measurement techniques or combining the PIV with a detection/trigging signal it may be possible to determine this frequency. One should of course keep in mind that one cannot expect a well-defined single frequency in a phenomenon like this, but rather a fairly broad-band peak.

The static wall pressure was measured at the spanwise centerline in the streamwise direction along the straight wall. An array of vortex generators was applied as a reference case of diffuser flow without separation. Comparing the two curves from flow with and without vortex generators clearly shows the separated region as a plateau present only in the case without vortex generators caused by the constriction of the outer flow by the separated region. The pressure coefficient at the measurement region outlet, achieved with vortex generators (0.80) is almost 10% higher than for the original case (0.72).

## 5. Acknowledgment

The authors would like to thank Ulf Landén for aiding in the manufacturing of the flow device and Kristian Angele for introducing us into the world of PIV. The Swedish Research Council and The Swedish Energy Agency are gratefully acknowledged for their financial support.

## References

Adrian, R. & Keane, R. 1992 Theory of cross-correlation in PIV. *Applied scientific research* **49**, 191–215.

Angele, K. P. 2002 Pressure-based scaling in a separating turbulent APG boundary layer. In *Advances in turbulence IX* (ed. I. Castro, P. E. Hancock & T. G. Thomas), pp. 639–642. CIMNE, Barcelona, Spain.

Baldi, S., Hann, D. & Yanneskis, M. 2002 On the measurement of turbulence energy dissipation in stirred vessels with PIV techniques. In *11th Int. Symp. on Applications of Laser Techniques to Fluid Mech.* Instituto superior técnico, Center for innovation, technology, and policy research, Lisbon, Portugal.

Brüger, A. 2002 Higher order methods suitable for direct numerical simulation of flows in complex geometries. *Tech. Rep.* 2002:07. Lic. thesis, Dept. of Mechanics, KTH, TRITA-MEK.

Brunet, L., Calzalbou, J. B., Chassaing, P. & Jervase, L. 1997 Experimental and computational study of pressure effects on turbulent flow in an asymmetric plane diffuser. In *11th Symp. on Turbulent Shear Flows, Grenoble, France*, pp. 114–119.

BUICE, C. U. & EATON, J. K. 1997 Experimental investigation of flow through an asymmetric plane diffuser. *Tech. Rep.*. Department of mechanical engineering, Stanford university.

BUICE, C. U. & EATON, J. K. 2000 Experimental investigation of flow through an asymmetric plane diffuser. *J. of Fluids Eng.* **122**, 433–435.

CHERRY, N. J., HILLIER, R. & LATOUR, M. E. M. P. 1984 Unsteady measurements in a separated and reattaching flow. *J. Fluid Mech.* **144**, 13–46.

COLLER, B. D., NOACK, B. R., NARAYANAN, S., BANASZUK, A. & KHIBNIK, A. I. 2000 Reduced-basis model for active separation control in a planar diffuser flow. In *AIAA Fluids 2000, 19-22 June 2000, Denver, CO, USA, AIAA-2000-2562*.

COMTE-BELLOT, G. 1965 Écoulement turbulent entre deux paroix parallèles. Publications scientifiques et techniques 419. Ministère de l'air, 2, Avenue de la Porte-d'Issy, Paris.

DIANAT, M. & CASTRO, I. P. 1991 Turbulence in a separated boundary layer. *J. Fluid Mech.* **226**, 91–123.

DURST, F., FISCHER, M., JOVANOVIĆ, J. & KIKURA, H. 1998 Methods to set-up and investigate low Reynolds number, fully developed turbulent plane channel flows. *ASME J. Fluids Eng.* **120**, 496.

EATON, J. K. & JOHNSTON, J. P. 1981 A review of research on subsonic turbulent flow reattachment. *AIAA J.* **19**, 1093–1100.

FISCHER, M., JOVANOVIĆ, J. & DURST, F. 2001 Reynolds number effects in near-wall region of turbulent channel flows. *Phys. Fluids* **13** (6), 1755–1767.

KALTENBACH, H.-J., FATICA, M., MITTAL, R., LUND, T. S. & MOIN, P. 1999 Study of flow in a planar asymmetric diffuser using large-eddy simulation. *J. Fluid Mech.* **390**, 151–185.

KIYA, M. & SASAKI, K. 1983 Structure of a turbulent separation bubble. *J. Fluid Mech.* **137**, 83–113.

OBI, S., AOKI, K. & MASUDA, S. 1993*a* Experimental and computational study of turbulent separating flow in an asymmetric plane diffuser. In *Ninth Symp. on Turbulent Shear Flows*, p. 305. Kyoto, Japan.

OBI, S., ISHIBASHI, N. & MASUDA, S. 1997 The mechanism of momentum transfer enhancement in periodically perturbed turbulent separated flow. In *2nd Int. Symp. on Turbulence, Heat and Mass Transfer, Delft, The Netherlands*, pp. 835–844.

OBI, S., OHIZUMI, K., AOKI, K. & MASUDA, S. 1993*b* *Turbulent separation control in a plane asymmetric diffuser by periodic perturbation*, pp. 633–642. Elsevier Science Publishers B.V.

PERRY, A. E. & FAIRLIE, B. D. 1975 A study of turbulent boundary-layer separation and reattachment. *J. Fluid Mech.* **69**, 657–672.

RAFFEL, M., WILLERT, C. & KOMPENHANS, J. 1997 *Particle Image Velocimetry, A practical guide*. Springer Verlag.

RUDERICH, R. & FERNHOLZ, H. H. 1975 An experimental investigation of a turbulent shear flow with separation, reverse flow, and reattachment. *J. Fluid Mech.* **163**, 283–322.

Simpson, R. L. 1989 Turbulent boundary-layer separation. *Ann. Rev. Fluid Mech.* **21**, 205–234.

# Paper 2

# Measurements in a plane asymmetric diffuser with 8.5° opening angle. Part II: Comparison with model predictions for turbulence characteristics

By Olle Törnblom, Björn Lindgren, Johan Gullman-Strand and Arne V. Johansson

Dept. of Mechanics, KTH, SE-100 44 Stockholm, Sweden

To be submitted

The separating turbulent flow in a plane asymmetric diffuser is studied experimentally. Careful measurements of the velocities have been made in all three spatial directions. The Reynolds number based on the inlet channel height and friction velocity was $Re_\tau$=2000. Emphasis is put on the study of the turbulence in the diffuser. The Reynolds-stress anisotropies and the corresponding anisotropy invariants are calculated and studied. The production terms in the transport equations for the Reynolds stresses are investigated. Comparisons with RANS-solutions using the Wallin & Johansson (2000) explicit algebraic Reynolds stress model (EARSM) are made. It is observed that the EARSM under-predicts the size of the separation bubble. The size of the predicted bubble is approximately 60% of the measured one and the main reason for this is the large level of wall-normal turbulence intensity predicted by the EARSM at the diffuser inlet.

## 1. Introduction

This is the second part of a study of the flow in an asymmetric plane diffuser with an opening angle of 8.5°. Here, we will concentrate our work on evaluating measurement data for quantities that are particularly interesting in turbulence modelling. The aim is to provide new insight into the dynamics that are essential in the modelling of this flow, and thereby help in testing existing models or in the development of new models. We will compare the measurement data with an Explicit algebraic Reynolds stress model (EARSM) calculation, based on the code presented in Gullman-Strand (2002).

The first part of this study entitled *Measurements in a plane asymmetric diffuser with an 8.5° opening angle. Part I: General flow characteristics* (Lindgren *et al.* (2002)) concentrated on the general flow characteristics of this

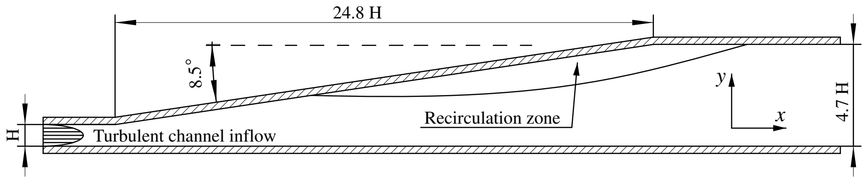

FIGURE 1. The measurement section of the wind-tunnel. A part of the inlet channel is seen to the left and part of the outlet channel is seen to the right.

diffuser flow such as mean velocity and turbulence intensity in the three spatial directions. It also includes measures of the extension of the separation bubble, its character and strength and the average pressure distribution. For information hereabout we refer to that paper. In this paper we focus on turbulence statistics which are compared with predictions based on RANS computations carried out by the third author.

The diffuser used in both these studies has one inclined wall with an opening angle of 8.5°. The opposite wall is straight, see figure 1. The diffuser is preceded by a 3.2 m channel with a height of 30 mm and a width of 1525 mm. This ensures fully developed turbulent channel flow as inlet condition into the diffuser (see *e.g.* Comte-Bellot (1965)). It is important when computations and experiments are compared, to have a well defined inlet condition. The diffuser is followed by a 2.5 m long outlet channel which is 141 mm high and 1520 mm wide. The purpose is here to minimize upstream influence from disturbances from other wind-tunnel parts located further downstream. The primary measurement techniques used are Particle Image Velocimetry in the streamwise wall-normal plane and Laser Doppler Velocimetry in the spanwise direction. An advantage of these measurement techniques is that they can measure both direction and absolute value of a fluid particle which is necessary when there is backflow involved. The Reynolds number based on the inlet channel height and the friction velocity is 2000.

The flow in the diffuser is characterized by a long thin separation bubble located at the inclined wall. The separation point is located about 9 channel heights downstream the diffuser inlet and the reattachment point is located 31 inlet channel heights downstream the inlet channel (see Lindgren *et al.* (2002)). The maximum thickness of the separation bubble is approximately 1.6 inlet channel heights occurring at the end of the diffuser.

Some numerical studies on this geometry have been performed previously. However, all these studies used a geometry with a larger opening angle (10°)

than that in the present study. An extensive numerical study of the plane asymmetric diffuser flow was made by Kaltenbach *et al.* (1999), who performed a large eddy simulation at a Reynolds number of 1000 based on the inlet channel height and the inlet friction velocity. Their data showed good agreement with the Buice & Eaton (1997) experimental data for velocity profiles. The point of separation also agreed well but some discrepancy was found in the location of the reattachment point. A possible reason for this can be the relatively small spanwise width of the computational domain which may tend to artificially enhance spanwise coherence of large scale structures. Kaltenbach *et al.* (1999) found that the sub-grid scale model plays an essential role to calculate the flow correctly, since sub-grid stresses are a major contribution to the wall-shear stress. The sub-grid scale model must also adapt to the increase in turbulence level in the downstream part of the diffuser.

Other numerical studies involving more or less advanced closures based on eddy-viscosity models, (differential) Reynolds stress models (RSM) and EARSM models have been performed by a number of research groups. For instance, Apsley & Leschziner (1999) tested a number of linear and non-linear eddy viscosity models as well as differential stress-transport models. They found that strain dependent coefficients and anisotropy resolving closures are needed. However no models tested were capable to resolve all flow features in the diffuser. Apsley & Leschziner (1999) also points out the possibility to encounter problems related to the "flapping" motion of the unsteady separation.

In an Ercoftac workshop (Hellsten & Rautaheimo (1999)), different numerical approaches with varying turbulence models were used and compared to the Buice & Eaton (1997) data-base. Models used comprised $k - \varepsilon$, $k - \omega$, RSM and LES. The agreement was, for the more simple models, in general fairly poor due to the complex flow in the diffuser.

The plane asymmetric diffuser has also been used as a test case for commercial codes. The investigation performed by Iaccarino (2000) aimed at finding the limits of the versatile commercial codes in this complex geometry. The codes tested were CFX, Fluent and Star-CD. Two turbulence models were tested, ($k - \epsilon$ and $\overline{v^2} - f$) for the three codes. The results were compared to the Obi *et al.* (1993) and Buice & Eaton (1997) data-bases. The $k - \epsilon$ model was unable to capture the recirculation zone but the $\overline{v^2} - f$ model did so with an accuracy in separation length of 6%. The agreement for the friction coefficient was also fairly good.

As is seen above, an ample amount of numerical tests of closures in plane asymmetric diffusers exists already today. Some of the major challenges in turbulence modelling are related to near-wall turbulence and pressure-gradient induced separation, phenomena which are represented in an ideally generic manner in the plane asymmetric diffuser flow. The present choice of opening angle ensures a separation-free flow near the straight wall, and the aspect ratio together with end-wall boundary layer control measures ensure a high degree of spanwise uniformity. This makes the present case ideal for detailed tests of turbulence modelling aspects that may require a high degree of accuracy in the turbulence statistics to evaluate differences in modelling approaches among high-level single-point closures, and sub-grid scale models in the LES-approach. The presently created data-base, containing information on all velocity components and related second order statistics, would, for instance, be well suited for tests of modern nonlinear RSM:s and newly developed approaches, including curvature corrections etc, within the concept of EARSM.

## 2. Turbulence models

### 2.1. *The RANS equations*

The by far most common approach to compute turbulent flows is to decompose the velocity and pressure field into a mean and a fluctuating part, and form equations for the mean velocity and single-point turbulence statistics. This approach is called the Reynolds decomposition and a detailed explanation of this standard technique can be found in *e.g.* Johansson & Burden (1999). The (incompressible) RANS equations,

$$\frac{\partial U_i}{\partial t} + U_j \frac{\partial U_i}{\partial x_j} = -\frac{1}{\rho}\frac{\partial P}{\partial x_i} + \frac{\partial}{\partial x_j}\left(2\nu S_{ij} - \overline{u_i' u_j'}\right) \tag{1}$$

$$\frac{\partial U_i}{\partial x_i} = 0, \tag{2}$$

which govern the ensemble averaged velocities ($U_i$) and the average pressure ($P$) are identical to the corresponding Navier-Stokes equations for the instantaneous velocities and pressure with one important exception, the Reynolds stress term. Since the flow considered is incompressible, we will consider the kinematic Reynolds stress tensor $-R_{ij} \equiv -\overline{u_i' u_j'}$, where $u_i'$ are the velocity fluctuations. The aim of single point closures is to construct a closed set of equations for this quantity, to be inserted into equations 1. An ensemble average is herein denoted with a bar over the respective quantity.

### 2.2. *Eddy-viscosity based two-equation models*

In CFD for engineering applications, the by far most commonly used method of closing the RANS set of equations is the eddy-viscosity based two-equation model approach. The eddy-viscosity hypothesis, introduced by the french physicist and mathematician V.J. Boussinesq in 1877, approximates the increased diffusivity due to turbulence by using a turbulent viscosity ($\nu_T$), analogous to the well known kinematic viscosity for a Newtonian fluid. Using the eddy-viscosity hypothesis the Reynolds stresses are approximated by

$$-\overline{u_i' u_j'} = 2\nu_T S_{ij} - \frac{2}{3} K \delta_{ij}. \tag{3}$$

Where $K \equiv \overline{u_i'u_i'}/2$ is the turbulence kinetic energy and $S_{ij} \equiv (U_{i,j} + U_{j,i})/2$ is the mean rate of strain tensor. By simple dimensional analysis it is easy to see that in order to estimate the turbulent viscosity one needs to know at least one time (or velocity) scale and one length scale of the turbulence. In so called two-equation models these scales are determined by solving transport equations for two turbulence quantities. Usually one of these quantities is the turbulence kinetic energy $K$ and the other can be *e.g.* the dissipation rate of turbulence kinetic energy $\varepsilon$, or the inverse timescale of the most energetic eddies $\omega$.

Such standard two-equation models can be reasonably accurate for predicting attached flows without large influences from mean flow streamline curvature or system rotation and the inclusion of two transport equations for turbulence quantities means that some history effects of the turbulence can be captured. In the Boussinesq hypothesis there is no dependence of the stresses on the rotation rate tensor ($\Omega_{ij} \equiv (U_{i,j} - U_{j,i})/2$), a deficiency which can influence the ability to predict *e.g.* separating flows. A more elaborate description of eddy-viscosity based two-equation models can be found in *e.g.* Wilcox (1993) and Johansson & Burden (1999).

### 2.3. *Differential Reynolds stress models (DRSM)*

A straightforward way to generalize the modelling approach as compared to the two-equation model approach, is to introduce the transport equations for the Reynolds stresses

$$\frac{DR_{ij}}{Dt} = \mathcal{P}_{ij} - \varepsilon_{ij} + \Pi_{ij} + \mathcal{D}_{ij}. \tag{4}$$

Such a model is referred to as a differential Reynolds stress model (DRSM) and pioneering work on this kind of model was done by Launder *et al.* (1975). Due to the symmetric nature of $R_{ij}$, six equations plus one for a turbulence 'length' scale, has to be solved in 3D flow problems. The production term $\mathcal{P}_{ij}$ is explicit in the Reynolds stresses and the mean velocity gradient tensor and does not have to be modelled within this modelling context.

The trace of the dissipation rate tensor $\varepsilon_{ij}$ is usually determined by an extra transport equation for $\varepsilon$ which is also used to determine the turbulent 'length' scale, and the anisotropy of the dissipation rate is often assumed to be negligible or modelled through use of the Reynolds stress anisotropies.

The pressure strain rate tensor $\Pi_{ij}$ is a correlation between the fluctuating pressure and the fluctuating strain rate. This term represents the intercomponent redistribution of the Reynolds stresses and its modelling is a key element in this type of closure. The models are based on solutions of the Poisson equation for the fluctuating pressure. The diffusion term $\mathcal{D}_{ij}$ is normally modelled with a gradient diffusion formulation.

In a DRSM much more of the turbulence physics are of course captured as compared to a two-equation eddy-viscosity model, but at the prize of five more equations to solve. As an alternative, the performance of a two-equation model can be improved if the eddy-viscosity approach is abandoned and the transport equations for the Reynolds stresses are approximated with an algebraic equation for the Reynolds stress anisotropy tensor.

### 2.4. *Explicit algebraic Reynolds stress models (EARSM)*

From equation 4 an equation for the Reynolds stress anisotropy tensor can be derived. The Reynolds stress anisotropy tensor is defined as

$$a_{ij} \equiv \frac{\overline{u_i' u_j'}}{K} - \frac{2}{3}\delta_{ij}. \tag{5}$$

Assuming that the flow is in so called 'weak equilibrium' one can discard the advection and diffusion terms in the transport equation for the anisotropy tensor. Weak equilibrium means that the timescale on which the anisotropy relaxes to some quasi-equilibrium state prescribed by the mean flow and the turbulent scales, is small. If the pressure-strain rate and dissipation rate anisotropy are modelled in terms of $S_{ij}$, $\Omega_{ij}$, $a_{ij}$ and the turbulence velocity and length-scales (*e.g.* $K$ and $\varepsilon$), the weak equilibrium assumption implies that the Reynolds stress anisotropy is completely determined by the local values of the mean strain and rotation rate tensors (normalized by the turbulence time scale), *i.e.*

$$f_{ij}(\mathbf{a}, \mathbf{S}^*, \mathbf{\Omega}^*) = 0. \tag{6}$$

Equation 6 represents an implicit relation between the anisotropy tensor ($\mathbf{a}$) and the normalized strain ($\mathbf{S}^*$) and rotation rate ($\mathbf{\Omega}^*$) tensors. The weak equilibrium assumption does not hold in slowly distorted turbulence where $\mathcal{P}/\varepsilon \ll 1$, *e.g.* in the outer part of a boundary layer or in the center of a jet or a channel-flow.

Using the weak equilibrium assumption together with isotropic assumption for the dissipation rate tensor and linear model for the pressure strain rate tensor one can derive an explicit algebraic equation for the anisotropy (see *e.g.* Gatski & Speziale (1993) and Wallin & Johansson (2000)), *i.e.*

$$a_{ij} = a_{ij}(\mathbf{S}^*, \mathbf{\Omega}^*). \tag{7}$$

This equation depends exclusively on the mean flow, or more precisely on the mean strain-rate and rotation-rate tensors. Such an expression requires very little effort to be evaluated, so the increase in computational effort for an EARSM compared to a standard two-equation model is almost negligible. The explicit expression is also a good way of ensuring robustness of the computational scheme.

The EARSM has several advantages over an ordinary eddy-viscosity based two-equation model, where

$$a_{ij} = 2C_\mu S^*_{ij}. \tag{8}$$

The EARSM has been shown to improve near-wall behavior and thereby reduce the need for near-wall damping, as compared to eddy-viscosity models. Effects of system rotation and streamline curvature can also be captured in the EARSM:s through extensions analyzed by *e.g.* Girimaji (1997) and Wallin & Johansson (2002). Curvature corrections are not included in the model used for comparisons herein.

## 3. Results

In this section results from the analysis of the turbulence data are presented and comparisons with computations are made. For a detailed description of the experiment, the mean flow and the Reynolds stresses, consult Lindgren *et al.* (2002) and for details on the computational aspects, consult Gullman-Strand (2002).

The numerical results have been obtained using a finite element code, created by an automated code generation procedure, first described by Amberg *et al.* (1999). The system of equations were the RANS equations with the EARSM by Wallin & Johansson (2000) combined with Wilcox low-Re $K - \omega$. The RANS equations were solved in a time-dependent fractional step scheme described by Guermond & Quartapelle (1997) and a decomposition of $\omega = \tilde{\omega} + \omega_w$ decreased the demand of grid resolution close to the walls. A more detailed description of the code generation procedure, formulation of the equations and solution strategy can be found in Gullman-Strand (2002).

The geometry used in the computations were identical to the experiments with respect to diffuser angle and height ratio but with inlet and outlet lengths of 10 $x/H$ and 60 $x/H$ respectively. The mesh was a structured triangular grid with 318 nodes in the streamwise direction, of which 100 were located in the diffuser and 75 nodes stretched in the wall-normal direction. The short inlet channel was possible since the turbulent channel inlet conditions were calculated by the same code but in a separate channel geometry, consistent with the guidelines of Hellsten & Rautaheimo (1999) for the 10° case.

To facilitate interpretation most of the data presented in this section have been plotted in the diffuser geometry, in all these plots the axis scales are $x/H$ and $y/H$ in the horizontal and vertical directions respectively, where $H$ is the inlet channel height. Velocities are normalized with $U_b$, being the inlet channel bulk velocity.

### 3.1. *Mean velocities*

A comparison of profiles of the streamwise average velocity can be seen in figure 2, the most noticeable difference between the computation and the measurements is that the separation bubble in the computation is much thinner. The maximum thickness of the recirculation zone is only 60% of that of the

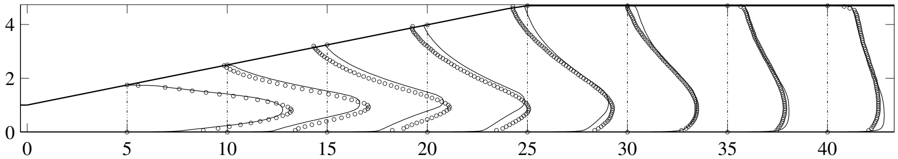

FIGURE 2. The mean velocity in the streamwise direction for experiment (∘) and EARSM (—); $10\frac{U}{U_b} + \frac{x}{H}$.

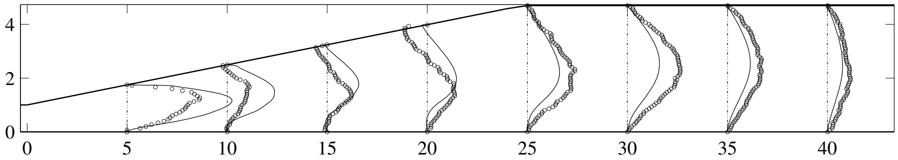

FIGURE 3. The mean velocity in the wall-normal direction for experiment (∘) and EARSM (—); $100\frac{V}{U_b} + \frac{x}{H}$.

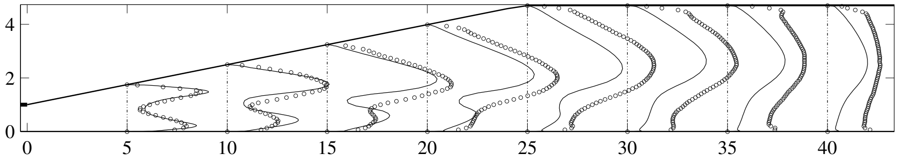

FIGURE 4. The turbulence kinetic energy for experiment (∘) and EARSM (—); $400\frac{K}{U_b^2} + \frac{x}{H}$.

measured separation. This discrepancy has a large influence on the whole flow-field. Since the smaller separation bubble constitutes a smaller displacement the whole flow-field is shifted towards the inclined wall as compared to the measured field. The experimentally determined separation point is located at $x/H = 9$ while in the computation it is at $x/H = 11$. The height of the computed bubble also grows much slower in the downstream direction than the measured. The reattachment points are located at $x/H = 31$ and $x/H = 27$ for the experiment and the computation respectively.

The wall-normal mean velocity in figure 3 is highly affected by the smaller separation zone in the simulation since the flow follows the inclined wall more closely. Accordingly it is larger than in the experiments in the diverging part of the diffuser and smaller in the exit channel where the flow is attached.

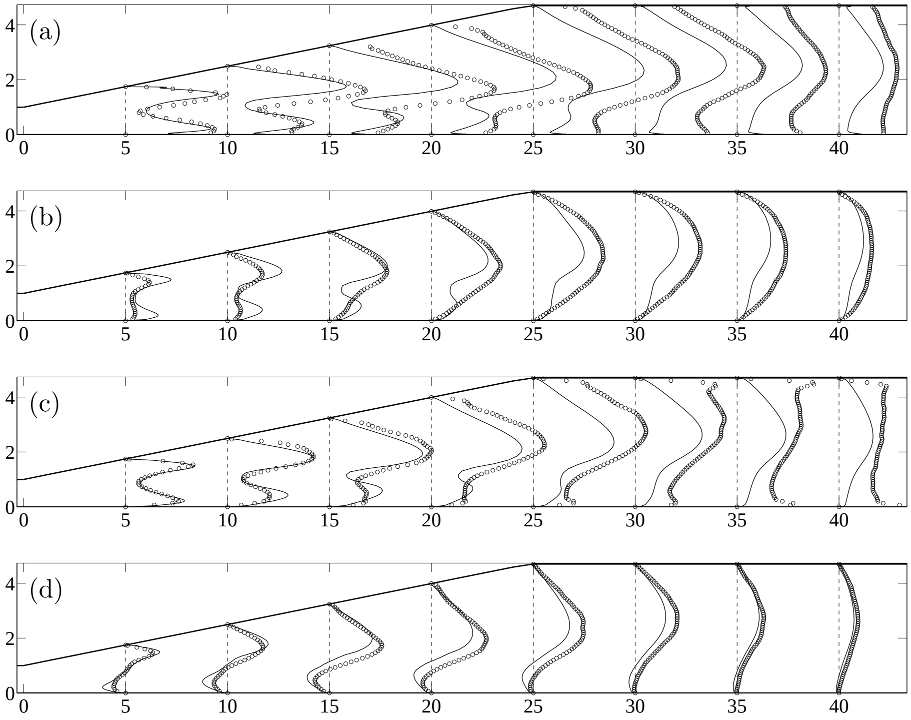

FIGURE 5. Measured (○) and computed (—) variance of turbulent fluctuations and Reynolds shear stress; (a) $\overline{u'^2}$, (b) $\overline{v'^2}$, (c) $\overline{w'^2}$ and (d) $\overline{u'v'}$, displayed as $500\frac{\overline{u'_i u'_j}}{U_b^2} + \frac{x}{H}$.

### 3.2. *Turbulence intensities and Reynolds shear stress*

There is good agreement for the turbulence kinetic energy $K$ (see Figure 4) at the first station, at $x/H = 5$, when neither the simulated nor the experimental flow has separated. The agreement then deteriorates further downstream. In general the turbulent kinetic energy is smaller in the simulation, something which might be attributed to the lower levels of shear in the region outside the separation bubble. The mean velocity profiles at $x/H = 35$ in figure 2 are very similar but the simulated $K$-levels at the same position are much smaller than the measured. This indicates that the supply of turbulent kinetic energy to this position from upstream positions is underestimated.

Looking closer into the components of $K$, shown in figure 5a–d, one can see that the computed $\overline{v'^2}$ is larger than the measured at the beginning of the

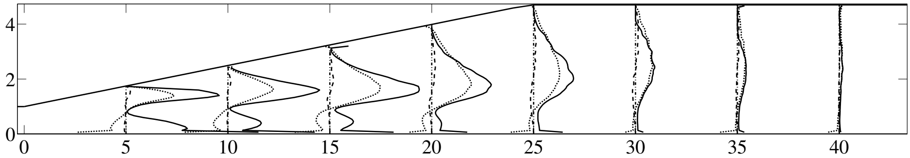

FIGURE 6. Measured Reynolds stress production rates; $\mathcal{P}_{11}$ (—), $\mathcal{P}_{22}$ (- - -) and $\mathcal{P}_{12}$ ($\cdots$), displayed as $1000\frac{\mathcal{P}_{ij}H}{U_b^3} + \frac{x}{H}$.

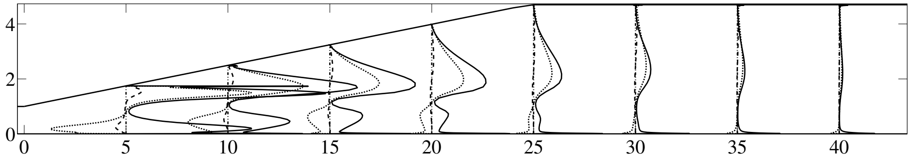

FIGURE 7. Calculated Reynolds stress production rates; $\mathcal{P}_{11}$ (—), $\mathcal{P}_{22}$ (- - -) and $\mathcal{P}_{12}$ ($\cdots$), displayed as $1000\frac{\mathcal{P}_{ij}H}{U_b^3} + \frac{x}{H}$.

diffuser, at the same location $\overline{u'^2}$ is slightly under-estimated in the computations while the peak heights of $\overline{w'^2}$ agree well. The experimental data show broader and higher variance peaks in the shear-layer over the separated region at the end of the diverging section than the computations, which is natural due to the larger separation bubble, while the peak near the plane wall is more accentuated in the computations. This is extra obvious in the profiles of $\overline{w'^2}$.The agreement of $\overline{u'v'}$ between the measurements and the computations is good except at the first two positions, where it is over-estimated in the computations near the inclined wall.

### 3.3. *Reynolds stress production*

The turbulent stresses in a flow produce new turbulence by interaction with the mean rates of strain and rotation

$$\mathcal{P}_{ij} = -\overline{u'_i u'_k}\frac{\partial U_j}{\partial x_k} - \overline{u'_j u'_k}\frac{\partial U_i}{\partial x_k}. \tag{9}$$

In the plane asymmetric diffuser flow, there is homogeneity in the spanwise direction, so only $\mathcal{P}_{11}$, $\mathcal{P}_{22}$ and $\mathcal{P}_{12} = \mathcal{P}_{21}$ are non-zero. Hence, all turbulent energy in the spanwise component ($\overline{w'w'}$), which is fairly high (see figure 5) has been redistributed from the two other components via the pressure strain rate term in equation 4, illustrating the importance of adequate modelling of $\Pi_{ij}$.

Figure 6 shows the three non-zero components of the production rate tensor. The highest production rates are found in the 11-component in the strong shear-layer above the separation bubble. This is due to the high level of mean

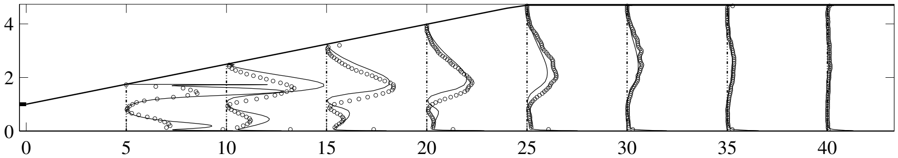

FIGURE 8. Turbulence kinetic energy production rate, $\mathcal{P}$; experiment (∘), EARSM (—), displayed as $1500\frac{\mathcal{P}H}{U_b^3} + \frac{x}{H}$.

shear ($\partial U/\partial y$) in combination with the peak in $\overline{u'v'}$ at this location *cf.* figure 5. Almost no production of the 11-component takes place at the location of the maximum peak for the streamwise velocity, which is consistent with the small mean shear in that region. For the $\mathcal{P}_{12}$-component the maximum peak is located at the same position as for the $\mathcal{P}_{11}$-component, also due to the high mean shear, but its strength is only about 60% of the 11-peak. The $\mathcal{P}_{12}$-component cross the zero level at the $y$-position where the streamwise mean velocity peaks and has a minimum in the 'boundary layer' on the straight wall. Compared to the other two components the $\mathcal{P}_{22}$-component is very small. At some locations this component attains negative values due to the deceleration of the flow along the plane wall. At the most downstream profile all production components are very small due to the very flat mean velocity profile here.

Figure 7 shows the computed components of the production rate tensor. All three components are significantly overestimated at the two most upstream positions, while the agreement is better further downstream.

In figure 8, a comparison is made for the production rates of turbulence kinetic energy ($\mathcal{P}$). In the first profiles at $x/H = 5$ and 10 the EARSM substantially overestimates the production rate. The peak levels are almost twice those of the experiment at the most upstream position. However, since the $K$ levels in this region agree well, the dissipation rate must also be overestimated. The shift of the EARSM profiles towards the inclined wall can, of course, be observed in $\mathcal{P}$ too. Further downstream the predicted production rate decreases in amplitude faster than the measured and this can explain why the produced quantity, $K$, is underestimated in the downstream part of the diffuser and in the exit channel.

### 3.4. *Reynolds stress anisotropy tensor*

The $a_{ij}$-tensor has two independent scalar measures which are invariant to the choice of coordinate system. These are defined as

$$II_a \equiv a_{ij}a_{ji} \quad \mathit{and} \quad III_a \equiv a_{ij}a_{jk}a_{ki}, \tag{10}$$

and are referred to as the second and third anisotropy invariants respectively. The experimental determination of these scalar measures is quite sensitive since

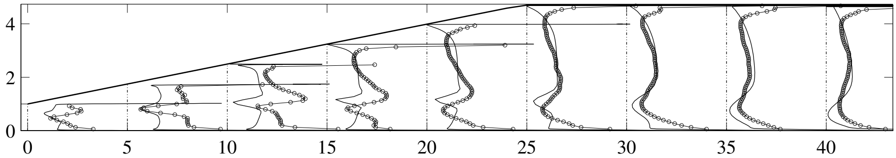

FIGURE 9. The second invariant of the turbulence anisotropy tensor for experiment (○) and EARSM (—); $5II_a + \frac{x}{H}$.

an error in the rms of the fluctuating velocity is taken to the fourth and sixth power in $II_a$ and $III_a$, respectively.

Figure 9 shows the variation of $II_a$ over the cross section at different streamwise positions in the diffuser. Throughout the whole diffuser $II_a$ has maxima near the walls due to the damping of the wall-normal turbulence intensity. A minimum is also found in all $II_a$-profiles at the same y-position as the maximum $U$-velocity. The low levels of shear here allows the turbulence to relax and become more isotropic. The position of the maximum in $II_a$ lies directly above the minimum in the positive $y$-direction. This is in between the locations of the maximum shear and the maximum velocity.

Figure 10 shows the four non-zero Reynolds stress anisotropy components. The streamwise component $a_{11}$ is generally the largest, the only exception to this is found far downstream close to the wall were the spanwise component is larger. The wall-normal component $a_{22}$ is negative at all positions, signifying a $\overline{v^2}$ content smaller than 2/3 of the kinetic energy. The perhaps most obvious discrepancy of the computed data in figure 11 as compared to the measurements is that the computed $a_{33}$ is identically zero making $a_{22}$ a mirror image of $a_{11}$, this approximation in the EARSM is not altogether valid for this flow according to the measurements.

The second invariant of the Reynolds stress anisotropy tensor $II_a$ is compared in figure 9. At the first station, where the computed profile of the turbulence kinetic energy agrees well with the experimental values, the second invariant is severely underestimated. The large difference between the streamwise and the wall-normal turbulence components (*c.f.* figure 10) is not captured correctly. The position and value of the minimum near the center is well predicted but the high levels of anisotropy on either sides of the minimum are underestimated. This underestimation of the anisotropy comes from an overestimation of the wall-normal velocity fluctuations ($v_{rms}$) by the EARSM in the region near the upstream corner of the inclined wall. The fact that the EARSM overestimates the $v_{rms}$, and also $\overline{u'v'}$ slightly, in the beginning of the diffuser is probably the reason for the delayed separation. This overestimation can in turn be a consequence of the omission of streamline curvature effects in this particular model. An addition of a curvature correction would reduce

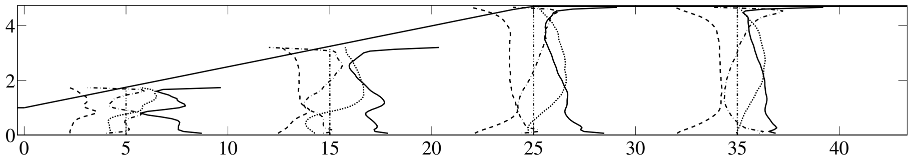

FIGURE 10. Measured Reynolds stress anisotropies; $a_{11}$ (—), $a_{22}$ (- - -), $a_{33}$ (- · -) and $a_{12}$ (· · ·), displayed as $5a_{ij} + \frac{x}{H}$.

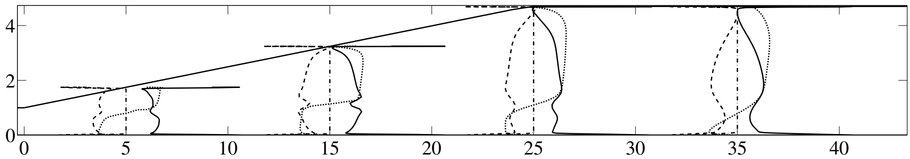

FIGURE 11. Computed Reynolds stress anisotropies; $a_{11}$ (—), $a_{22}$ (- - -), $a_{33}$ (- · -) and $a_{12}$ (· · ·), displayed as $5a_{ij} + \frac{x}{H}$.

the turbulence levels near the upstream corner of the inclined wall. Further downstream at the stations $x/H$ =10–25 the maximum values of the experimental anisotropy is gradually decreased and the quantitative agreement with the computations is increased, but on the other hand the discrepancy in the location of the minimum peak increases due to the smaller separation bubble in the computation. The best agreement is found at the most downstream stations in the exit channel, but the behavior close to the walls is, as in all profiles, quite different. The measured second invariant increases more slowly with increasing distance from the walls as compared to the computed invariant.

The pressure distributions on the plane wall are plotted in 12, normalized with a dynamic pressure based on the inlet channel bulk velocity. They clearly reflect the difference in strength of the separation. The EARSM gives a slightly higher pressure recovery than the experiment and the effects of displacement by the separation bubble are much smaller.

## 4. Concluding remarks

The plane asymmetric diffuser with 8.5° opening angle has shown to be a challenging flow case for turbulence model testing with several important phenomena, *e.g.* flow separation and reattachment, highly anisotropic turbulence, high levels of turbulence and some streamline curvature effects. These complex flow phenomena all occur within a relatively simple two-dimensional geometry. The smaller angle of the diffuser compared to that (10°) in the earlier experiments by Obi *et al.* (1993) and Buice & Eaton (2000) seems to give a separation which is even more difficult to predict and hence constitutes a truly challenging test case for turbulence closures.

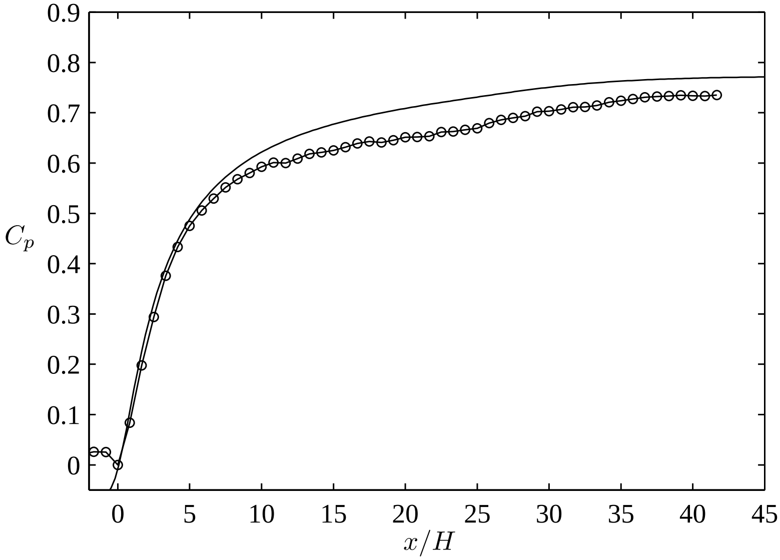

Figure 12. Comparison between the measured pressure distribution (○) and the EARSM (—).

The data-base of measurements has proven to be useful for comparison with computations, but more data from the near-wall regions are desirable. Especially in the region near the upstream corner of the inclined wall where streamline curvature is suspected to influence the turbulence. Furthermore, Kaltenbach *et al.* (1999) noted in an LES-calculation that a very small separated region formed in the viscous layer in this region. Accurate modelling and fine resolution of the flow in this region is crucial in order to obtain the correct behavior of the separating boundary layer on the inclined wall.

The EARSM manages to predict a separation bubble, but the size of it is not in close agreement with the measurements. The main reason for this is believed to be the overestimation of $v_{rms}$ and $\overline{u'v'}$ in the beginning of the diffuser. This can be related to the above-mentioned complicated flow in this region. The curvature correction described in Wallin & Johansson (2002) has not been implemented in the EARSM with which the comparisons are made. Adding curvature corrections would reduce the overestimated Reynolds-stress components at the inclined wall. History effects related to advection of the anisotropy along streamlines may also be of influence here. To account for these a DRSM modelling approach would be the normal choice.

However, Apsley & Leschziner (1999) tested four different DRSM:s on the 10° case, two of the models used wall functions and two were low Reynolds number models, without getting satisfying results. It was argued that the difficulties related to the modelling of the wall-asymptotic behavior could be a reason. This would indicate that a DRSM with nonlinear models for $\Pi_{ij}$ etc. would be interesting for this case. The DRSM of Sjögren & Johansson (2000) is such a model that has been proven to satisfy near-wall asymptotic behaviors through satisfaction of strong realizability. Apsley & Leschziner (1999) also mention the possible problem of periodic shear-layer instabilities provoked by the upstream corner of the diffuser as a reason for the general failure of all models to resolve the initial development of the boundary layer on the inclined wall.

## 5. Acknowledgement

The authors would like to thank Ulf Landén for aiding in the manufacturing of the wind-tunnel and measurement equipment. The Swedish Research Council, The Swedish Energy Agency and the Integral Vehicle Structures research school are gratefully acknowledged for their financial support.

## References

Amberg, G., Törnhardt, R. & Winkler, C. 1999 Finite elemet simulations using symbolic computing. *Mathematics and Computers in Simulation* **44**, 275–274.

Apsley, D. D. & Leschziner, M. A. 1999 Advanced turbulence modelling of separated flow in a diffuser. *Flow, Turbulence and Combustion* **63**, 81—112.

Buice, C. U. & Eaton, J. K. 1997 Experimental investigation of flow through an asymmetric plane diffuser. *Tech. Rep.*. Department of mechanical engineering, Stanford university.

Buice, C. U. & Eaton, J. K. 2000 Experimental investigation of flow through an asymmetric plane diffuser. *J. of Fluids Eng.* **122**, 433–435.

Comte-Bellot, G. 1965 Écoulement turbulent entre deux paroix parallèles. Publications scientifiques et techniques 419. Ministère de l'air, 2, Avenue de la Porte-d'Issy, Paris.

Gatski, T. B. & Speziale, C. G. 1993 On explicit algebraic stress models for complex turbulent flows. *J. Fluid Mech.* **254**, 59–78.

Girimaji, S. S. 1997 A Galilean invariant explicit algebraic Reynolds stress model for turbulent curved flows. *Phys. Fluids* **9**, 1067–1077.

Guermond, J. L. & Quartapelle, L. 1997 Calculation of incompressible vicous flow by an unconditionally stable projection FEM. *Journal of Computational Physics* **132** (CP965587), 12–33.

Gullman-Strand, J. 2002 Turbulence modeling using automated code generation applied to asymmetric diffuser flow. Dept. of mechanics, KTH, Stockholm, Sweden, licentiate thesis.

Hellsten, A. & Rautaheimo, P., ed. 1999 *Workshop on refined turbulence modelling*. ERCOFTAC/IAHR/COST.

IACCARINO, G. 2000 Prediction of the turbulent flow in a diffuser with commersial CFD codes. *Tech. Rep.*. Center for Turbulence Research.

JOHANSSON, A. V. & BURDEN, A. D. 1999 An introduction to turbulence modelling. In *Transition, Turbulence and modelling* (ed. A. Hanifi, P. Alfredsson, A. Johansson & D. Henningsson), chap. 4. Kluwer academic publishers.

KALTENBACH, H.-J., FATICA, M., MITTAL, R., LUND, T. S. & MOIN, P. 1999 Study of flow in a planar asymmetric diffuser using large-eddy simulation. *J. Fluid Mech.* **390**, 151–185.

LAUNDER, B., REECE, G. & RODI, W. 1975 Progress in the development of a Reynolds-stress turbulence closure. *J. Fluid Mech.* **68**, 537–566.

LINDGREN, B., TÖRNBLOM, O. & JOHANSSON, A. V. 2002 Measurements in a plane asymmetric diffuser with 8.5° opening angle. part I: General flow characteristics. *To be submitted* .

OBI, S., AOKI, K. & MASUDA, S. 1993 Experimental and computational study of turbulent separating flow in an asymmetric plane diffuser. In *Ninth Symp. on Turbulent Shear Flows*, p. 305. Kyoto, Japan.

SJÖGREN, T. & JOHANSSON, A. V. 2000 Development and calibration of algebraic nonlinear models for terms in the Reynolds stress transport equations. *Phys. Fluids* **12** (6), 1554–1572.

WALLIN, S. & JOHANSSON, A. V. 2000 An explicit algebraic Reynolds stress modell for incompressible and compressible turbulent flows. *J. Fluid Mech.* **403**, 89–132.

WALLIN, S. & JOHANSSON, A. V. 2002 Modeling streamline curvature effects in explicit algebraic Reynolds stress turbulence models. *Int. J. of Heat and Fluid Flow.* **23**, 721–730.

WILCOX, D. C. 1993 *Turbulence modeling for CFD*. DCW Industries Inc., USA.

# Paper 3

# Design and calibration of a plane asymmetric diffuser wind-tunnel

By Olle Törnblom, Björn Lindgren and Arne V. Johansson

Dept. of Mechanics, KTH, SE-100 44 Stockholm, Sweden

The design process of an experimental setup for studying a plane asymmetric diffuser flow is described. Prior to the diffuser the flow passes through a 3 m long and 30 mm high channel to generate a turbulent channel flow as inlet condition to the measurement section, which is a plane asymmetric diffuser. The opening angle of the inclined diffuser wall can be adjusted between 8-10° in order to be able to set the size of the separated region, within a limited range. The wind-tunnel is of closed circuit type in order to allow for flow seeding in an indoor environment. The wind-tunnel is driven by an 11 kW radial fan, capable of generating inlet channel flow Reynolds numbers of up to $HU_{cl}/\nu$ =60000, $H$ being the channel height and $U_{cl}$ the channel centerline velocity. The calibration of the wind-tunnel is described and special attention is paid to the two-dimensionality of the flow and the long time variations of the wind-tunnel velocity.

## 1. Introduction

Study of diffuser flows, *i.e.* duct flows subjected to an adverse pressure gradient, is motivated by the large number of applications in which these flows appear and the energy savings that may result from an increased knowledge about proper diffuser designs and separation control. The experimental facility for which the design is described herein was built to study a generic flow with separation, both in order to get a database for turbulence model comparisons as well as to test separation control techniques.

If one desires to study turbulent separating flow, separation control and provide reference data for computations, in the same geometry, it has to be chosen with care. The most generic way to study separation is to do a flat plate experiment where an adverse pressure gradient is produced by altering the free-stream velocity with a variable geometry of the opposing wind-tunnel wall (see *e.g.* Perry & Fairlie (1975) and Angele (2002)). Dianat & Castro (1991) used a porous cylinder with a small flap at the trailing edge mounted above a flat plate to generate the pressure gradient. Another category of separated flows is that associated with sharp edges or bluff body geometries. Examples are

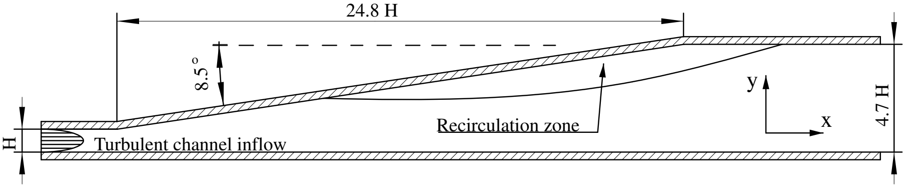

FIGURE 1. The plane asymmetric diffuser.

flow over flat plates or cylinders with blunt leading edges (*e.g.* Cherry *et al.* (1984) and Ruderich & Fernholz (1975)) or flow over a backward facing step (*e.g.* Etheridge & Kemp (1978) and Yoshioka *et al.* (2001)). Symmetric diffuser flows have been investigated by *e.g.* Sovran & Klomp (1967) and Chithambaran *et al.* (1984). All of these flow cases have been used to study different aspects of separation, but some are more suited for the study of generic mechanisms and comparison between experiments and numerical simulations. For instance the varying free-stream velocity in a separating flow on a flat plate can be difficult to mimic accurately in a CFD simulation. In blunt edge flows and flows over backward facing steps the challenge of predicting the separation point vanishes, as the separation inevitably will occur at the corner. In symmetric diffusers the separation can fluctuate between the two diffuser walls in a random manner and at long time-scales making ensemble averaging a very tedious task. In a CFD calculation, this unstable flow situation may also cause convergence problems.

The plane asymmetric diffuser with turbulent channel inflow, shown in figure 1, had the properties we were looking for. The fully developed turbulent channel flow used as inflow condition is a well known flow, simplifying the task of setting appropriate boundary conditions, both in CFD computations and in direct numerical simulations. The asymmetric geometry favors separation on the inclined wall and eliminates the problems associated with symmetric diffusers. If the upstream corner of the inclined wall is sufficiently smooth with a finite radius of curvature, the separation point will be located at the inclined wall, giving a challenging flow to predict in simulations and a location of the separation point sensitive to control. Furthermore, the relatively simple geometry with two dimensional flow and mostly straight walls facilitate CFD grid generation and the determination of positions inside the measurement section.

## 2. Design

### 2.1. *Pre-design considerations*

At the time when the first design steps where taken, there existed two (to the authors known) previous experiments in a very similar geometry *i.e.* those by

Obi *et al.* (1993) and Buice & Eaton (1997). In particular the latter one, which contains a detailed description of the experimental setup, was studied in order to learn about the difficulties related to the design of a plane asymmetric diffuser experiment. The major difficulty of this flow case is the inherent tendency, of a separating flow, to be three-dimensional. Since we required the flow to be two-dimensional (in an average sense), the three-dimensional behavior must be controlled. Since three-dimensional effects enter the flow via the end walls (the walls which limit the spanwise extent of the diffuser), the ideal, but unrealistic, solution would be to have an infinitely wide diffuser. However, a relatively large spanwise width compared to the height of the diffuser (*i.e.* a large aspect ratio) is a necessary requirement to have a two dimensional flow field.

A preliminary idea was that the newly built low speed wind-tunnel at the department (*cf.* Lindgren & Johansson (2002)) could be used for the experiment. But that alternative was abandoned due to the large pressure losses that the inlet channel would cause and because of the limited aspect ratio it would allow.

Another decision which needs to be taken before the actual design-work start is how large the diffuser should be. The size of the facility partly determines what Reynolds number the flow will have and also what fan power is needed to drive the wind-tunnel at the desired flow speeds. In a small facility the flow will be more influenced by small imperfections in the design *e.g.* small edges in joints between different wall sections. A too small test-section also limits the accessibility, due to the physical size of our hands, arms etc. and it also requires better precision in the positioning of the measurement probe than in a larger test-section, for the same relative error.

With these arguments in mind we decided to make our diffuser larger than the ones used in the experiments by Obi *et al.* (1993) and Buice & Eaton (1997). We also wanted a larger aspect ratio than the previous experiments. Obi's and Buice's inlet channel heights were 20 mm and 15 mm and their spanwise widths were 700 mm and 450 mm respectively. We chose to build a 30 mm high channel and an inlet aspect ratio of 50, giving a channel width of 1500 mm (due to the standard width of plywood sheets the final channel was built with a width of 1525 mm). In turbulent channel flow an aspect ratio of five is the lowest possible in order to have (a reasonably) two-dimensional flow in an about two channel heights wide region in the center of the channel (Johansson & Alfredsson (1986)). If the aspect ratio is lower than this, secondary flow effects caused by end walls and corners may influence the flow. In our facility this requirement is well fulfilled also in the exit channel where the aspect ratio is 10.8. However, in flows with adverse pressure gradients these rules of thumb can only be considered valid if separation is avoided on the end walls.

In order to produce a fully developed turbulent channel flow it was decided that the length of the inlet channel should be at least 100 channel heights. According to the experiments by Comte-Bellot (1965) the higher order statistical moments are fully developed at 60 channel heights from the inlet. Similar observations were made by Johansson & Alfredsson (1982).

Accordingly, the final choice of channel geometry was a 30 mm high, 3000 mm long and 1500 mm wide channel. It was concluded that, in order to minimize the floor area occupied by the wind-tunnel, the channel should be built so that the spanwise direction was oriented vertically, which is also favorable in the sense of minimizing wall deflections caused by gravity.

One of the obvious difficulties when studying separating flows experimentally is the occurrence of velocities with changing sign, due to the region of backflow. This difficulty makes it impossible to measure with hot-wire anemometry, an otherwise well established and accurate technique. If one wants to determine both the value of the velocity and its direction one has a few alternatives; pulsed hot-wires, laser doppler velocimetry (LDV) or particle image velocimetry (PIV). The natural choice for us was to use the two latter techniques, as these techniques are well established at our department and complement each other well, LDV gives rather high data rates for accurate point measurements and PIV gives whole field measurements but at a slow rate. LDV and PIV are both optical methods, and thereby require optical access to the flow. Hence, the measurement section of the wind-tunnel has to be made in a transparent material. If one wants to make a large transparent wall, as in a wind-tunnel test section, at a reasonable cost one has practically two choices, window glass or polymer glass. Window glass typically has a more even and precise thickness than polymer glass. An even thickness is of high importance when measuring with LDV, since a distortion of the laser-beams (or rather of one of the beams) can make them misaligned in the measurement volume, resulting in bad, or no, doppler signals. Furthermore, window glass has a higher modulus of elasticity as compared to polymer glass which allows thinner sheets to be used for a certain desired stiffness. Thinner sheets will also contribute to lowering the optical distortion. If one desires to use polymer glass a popular choice is Plexiglas® which is made from polymethyl methacrylate (PMMA). This material is usually cheaper than window glass and not as brittle, furthermore it is easier to machine than window glass. Another material property which could influence the choice is the refractive index, but for PMMA and window glass this can be disregarded since it is approximately 1.5 for both materials. The need to be able to drill pressure taps, the cheaper prize and the possibility to join Plexiglas® sheets together with screws made us choose this material for large parts of the measurement section.

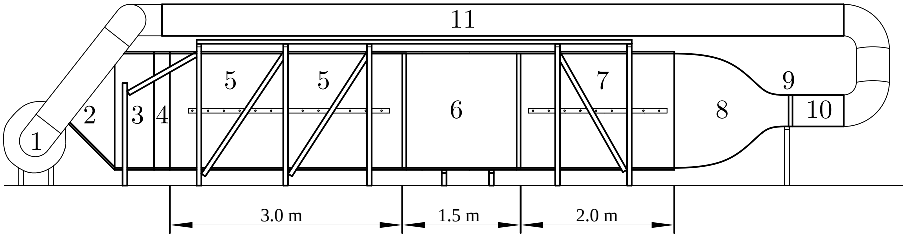

FIGURE 2. A sketch of the complete wind-tunnel. Refer to table 1 for a description of the numbered parts.

| Part | Description |
|---:|---|
| 1 | Fan, 11 kW centrifugal |
| 2 | Transformer from 322×229 mm$^2$ to 1525×100 mm$^2$ |
| 3 | Settling chamber, 1525×100×500 mm$^3$ |
| 4 | Contraction, from 1525×100 mm$^2$ to 1525×30 mm$^2$ |
| 5 | Inlet channel, 1525×30×3000 mm$^3$ |
| 6 | Diffuser/measurement section, from 1525×30 mm$^2$ to 1525×141 mm$^2$ |
| 7 | Exit channel, 1525×141×2000 mm$^3$ |
| 8 | Contraction, from 1525×141 mm$^2$ to 400×300 mm$^2$ |
| 9 | Heat exchanger |
| 10 | Transformer, from 400×300 mm$^2$ to 400 mm diameter |
| 11 | Return pipe, 400 mm diameter with five 90° bends |

TABLE 1. Description of the numbered parts in figure 2.

### 2.2. *Fan and motor*

Having decided the spanwise width and height of the inlet channel and the desired $Re_\tau$ in the inlet channel the required flow rate can be calculated using the logarithmic friction law and Dean's relation,

$$\frac{U_{cl}}{u_\tau} = \frac{1}{\varkappa} \ln\left(\frac{u_\tau H}{2\nu}\right) + C \tag{1}$$

$$\frac{U_{cl}}{U_b} = 1.28 \left(\frac{U_b H}{2\nu}\right)^{-0.0116} \tag{2}$$

with the additive constant $C = 6.0$ and $\varkappa = 0.4$. Where $U_{cl}$ is the channel centerline velocity, $u_\tau$ the friction velocity at the wall, $U_b$ the channel bulk velocity and $H$ is the channel height. A desired $Re_\tau = u_\tau H/\nu = 4000$ gives, according to these relations and the chosen channel area, a volume flux of approximately 1.8 m$^3$/s. In order to choose a fan one has to know also at what pressure the required flow should be delivered. This has to be estimated. A very rough estimate yielded that the wind-tunnel would cause pressure losses corresponding to approximately three times the dynamic pressure of the inlet channel bulk velocity. Later this estimate was proven to be reasonably accurate for the first design, which did not have a return circuit and heat exchanger. When choosing a fan it is advisable to examine not only the maximum performance, but also the performance over a region of the fan characteristics curve. It is desirable to have a characteristics curve in the volume flow region where the fan will be used, that gives as small a flux variation as possible for a given variation in the pressure, for instance due to a nonstationary separation bubble.

Based on these estimates a centrifugal fan capable of delivering 2.1 $\mathrm{m}^3/\mathrm{s}$ at 3000 Pa was ordered from Ventur tekniska AB. To control the speed of the 11 kW induction motor, the fan was complemented with a frequency converter and a filter, from ABB Motors AB.

### 2.3. *Transformer and settling chamber upstream the channel*

The fan has an outlet section of $322\times229\ \mathrm{mm}^2$ that has to be transformed into the large aspect ratio cross-section ($1525\times30\ \mathrm{mm}^2$) of the inlet channel. This transformation had to take place over a limited length, putting high demand on the design in order to minimize losses and ensure an even flow over the whole cross-section.

A common way to achieve a spanwise homogeneous flow is to have a settling or stagnation chamber, with large cross-section area where the velocity is very low, followed by a contraction into the channel. Here, we chose to have a rather small settling chamber with a cross-section area of $1525 \times 100\ \mathrm{mm}^2$. By doing so, the transformer between the fan and the settling chamber will have a shape which diverges in the spanwise direction and contracts in the other direction, see figure 3. The total expansion ratio, *i.e.* the ratio between the cross-section area of the settling chamber and the fan outlet area, is thus only about two. Two splitter plates are mounted immediately after the fan outlet to avoid large scale flow separation here and to direct the flow outwards in the spanwise direction.

Three screens, shown in figure 3, were placed in the transformer and settling chamber in order to even out mean flow variations. The screens used have a wire diameter $d$ of 0.71 mm and a (wire center to wire center) mesh width $M$ of 3.2 mm. These values give a porosity $\beta = (1 - d/M)^2 = 0.6$. Using screens will not only even out mean flow variations but also reduce angle deviations relative to the screen according to the relation

$$\phi = \alpha\theta, \tag{3}$$

where $\theta$ is the angle of the incoming flow and $\phi$ the angle of the out-going flow. The constant $\alpha$ is related to the local pressure-loss coefficient $K_0$ through the

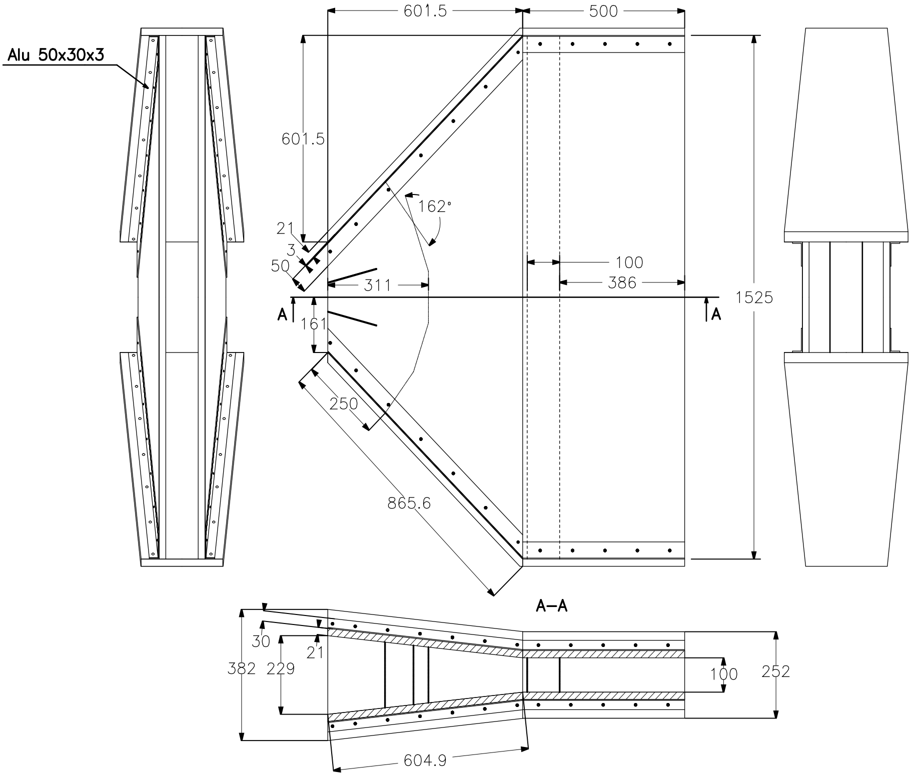

FIGURE 3. Four view drawing of the transformer and settling chamber upstream the channel.

empirical relation (see Laws & Livesey (1978))

$$\alpha = \frac{1.1}{\sqrt{1+K_0}}. \tag{4}$$

The local pressure-loss coefficient is highly Reynolds number dependent for subcritical Reynolds numbers but can for higher Reynolds numbers be approximated with

$$K_0 = 0.5\frac{1-\beta^2}{\beta^2}, \tag{5}$$

if $0.6 < \beta < 0.7$. With a volume flow of 2.1 $\mathrm{m}^3/\mathrm{s}$ the wire-diameter Reynolds number will be well above the critical value of $Re_d = 100$. Using equations 4 and 5 it can be seen that the local pressure-loss coefficient will be $K_0 = 0.9$ and that an error in the incoming flow angle relative to the screen will be reduced by a factor 0.8 after the screen. Streamwise mean velocity variations are reduced when the flow passes through a screen according to the expression

$$\frac{\Delta u_2}{\Delta u_1} = \frac{1 + \alpha - \alpha K_0}{1 + \alpha + K_0}, \tag{6}$$

derived by Taylor & Batchelor (1949), where $\Delta u_1$ and $\Delta u_2$ are the variations of the streamwise mean velocity upstream and downstream the screen respectively. For the screens of concern herein this ratio will be 0.4.

In the diffusing part, a bent screen was used in order to both even out mean velocity variations and to direct the flow towards the desired direction according to equation 3. Further downstream, in the first part of the settling chamber, two screens are placed to further reduce possible mean flow variations. The screens were mounted onto frames made from 15×15 mm stainless steel tubes and were manufactured by AB Derma in Gråbo, Sweden.

Both the transformer and the settling chamber were manufactured in plywood sheets joined together with L-shaped aluminum profiles and screws and sealed with tightening material. All the wind-tunnel parts are mounted in a framework (as can be seen in figure 2) of 60×40×3 $\text{mm}^3$ and 60×40×4 $\text{mm}^3$ steel tubes and steel L-profiles respectively. The steel framework is bolted to the concrete floor in the laboratory.

### 2.4. *Contraction and inlet channel*

The settling chamber is followed by a two-dimensional contraction, changing the channel height from 100 mm to 30 mm. The shape of the contraction, shown in figure 4, is described by two sinus hyperbolic functions as described in Lindgren & Johansson (2002). This shape is an optimal shape regarding the pressure gradient along the walls and it was derived originally for the MTL wind-tunnel by Henrik Alfredsson and Alexander Sahlin at the department, using inviscid/boundary layer calculations. The contraction was manufactured in polystyrene foam which was cut to the appropriate shape using a hot-wire saw. The polystyrene foam was covered with a glassfiber-epoxy laminate in order to have a smooth and hard surface.

The inlet channel consists of two 3000×1525×21 $\text{mm}^3$ plywood sheets with plywood end walls joined together with L-shaped aluminum profiles. Four L-shaped aluminum profiles oriented in the spanwise direction are screwed to the large plywood sheets in order to prevent the walls from bulging due to the larger pressure inside the channel. Furthermore, the large plywood sheets are supported along their centerlines with adjustable screws in order to ensure a constant (30 mm) channel height at all locations. The channel height was controlled with a movable 30 mm plastic cube (mounted on a long stick to be able to reach all points in the channel) and adjusted with the screws. The horizontal bar with the adjustment screws can be seen in figure 2.

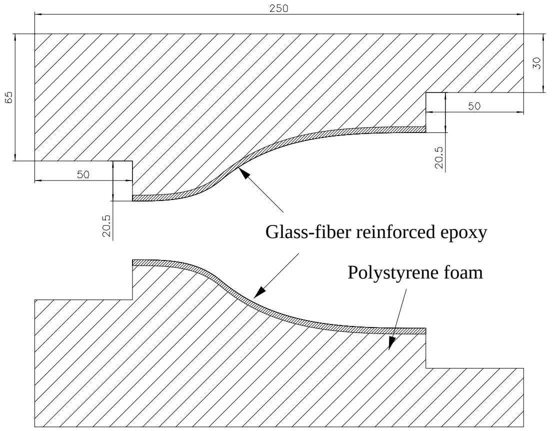

FIGURE 4. The design for the contraction before the inlet channel

### 2.5. *Measurement section*

The measurement section (part number 6 in figure 2) is connected to the inlet channel and the exit channel with high precision joints milled in aluminum with steel guide taps. The joints are held together with three DE-STA-CO® clasps at each side. This design allows the measurement section to be removed in order to facilitate modification of the diffuser or measurement installations.

As mentioned in section 2.1, optical access to the measurement section is necessary and Plexiglas® was believed to be the most appropriate transparent material. The plane wall of the measurement section was made from a single 1500×1525×25 $\mathrm{mm}^3$ Plexiglas® sheet and the end walls are two 350×1500×25 $\mathrm{mm}^3$ sheets. It was discovered that the delivered Plexiglas® varied in thickness as much as ±1 mm, and later on a 4 mm thick float-glass window was inserted to replace the Plexiglas® in the upper end wall. The 1250×155 $\mathrm{mm}^2$ piece of float-glass was taken from the mid portion of a large glass plate where the thickness homogeneity are best according to a representative for Pilkington floatglas AB in Halmstad, Sweden. The plane wall and the end walls are joined with screws that go through the end walls and are screwed into threaded holes in the plane wall.

The inclined wall of the measurement section is made as an aluminum sandwich construction. Square tubes (20×20 $\mathrm{mm}^2$) are screwed and glued with epoxy to a 4 mm sheet of aluminum. A 1 mm thick sheet of aluminium is then glued onto the 4 mm sheet to have a smooth surface. The smooth transitions between the inlet channel and the inclined wall and between the inclined wall and the straight wall in the exit channel are achieved by omitting the 4 mm sheet in these areas and letting the 1 mm sheet bend to form a smooth curve. This design allows the angle of the inclined wall to be changed

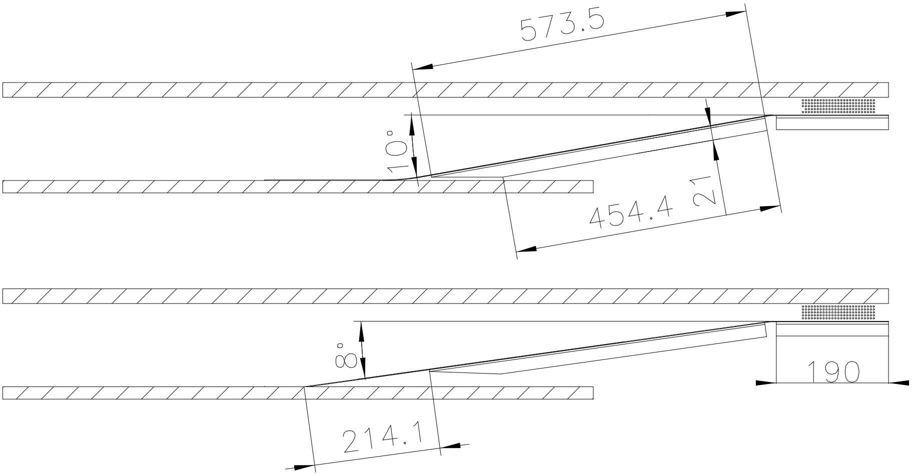

Figure 5. Cross section of the measurement section showing the design of the inclined wall and between which angles the diffuser can be altered. The holes for end wall boundary layer removal can also be seen.

between approximately 8° and 10°, see figure 5. The inclined wall is fastened to a framework through adjustable screws which are used to alter the angle of the inclined wall. The inclined wall can be adjusted to the desired angle with high accuracy by inserting precision-milled blocks with correct angle into the measurement section and adjusting the screws. The flat wall in the measurement section downstream the inclined wall is made of 21 mm thick plywood and has two hatches that allow easy access to the measurement section.

When the turbulent channel flow develops in the 3 m long inlet channel boundary layers will form on the channel end walls. These boundary layers will decrease the level of momentum in a region near the end walls, making the end wall flow sensitive to adverse pressure gradients. By reducing the thickness of the end wall boundary layers through suction before the diffuser where the adverse pressure gradient starts, end wall separation can be avoided. The suction is applied through a 100 mm long perforated section of the end wall ending 50 mm before the diffuser starts. The suction is produced by a separate fan connected to the perforated parts through hoses. The air that is sucked out is brought back to the wind-tunnel circuit by leading the exit of the fan to a connection on the return channel. After the perforated section a new boundary layer will start to grow and to prevent this boundary layer from separating small vortex generators are put on the end walls in the diffuser.

A row of 57 pressure taps were drilled along the centerline of the plane wall, the distance between the pressure taps is 25 mm and the holes which are drilled directly in the Plexiglas® has a diameter of 0.4 mm. Similarly a courser row of pressure holes were drilled on the opposite side of the diffuser, along the inclined wall. Pressure taps were also drilled in spanwise rows on both walls 100 mm before the upper corner of the diffuser in order to measure the spanwise homogeneity of the incoming flow.

### 2.6. *Exit channel and transformer before the heat exchanger*

The exit channel is built in plywood in a similar way as the inlet channel and has the purpose of reducing the effects of the downstream wind-tunnel parts on the flow in the measurement section. The size of the exit channel is $2000 \times 1525 \times 141$ mm$^3$ and stiffening aluminum L-profiles and adjustment screws along the centerline are used, in the same fashion as for the inlet channel, to ensure that these dimensions are kept.

The exit channel is followed by a transformer, changing the cross section to $400 \times 300$ mm$^2$ in order fit the dimensions of the following heat exchanger. The shape of the contraction was determined using the same formula as for the contraction upstream the inlet channel (see section 2.4). Since the transformer is contracting in one direction and expanding in the other the total contraction ratio is only 1.8, smaller than what one can conceive from figure 2. The sides of the transformer were sawed into the proper shape from a 25 mm thick plywood sheet and the (bent) upper and lower walls were made by steel tinplates nailed to the plywood.

### 2.7. *Heat exchanger and return channel*

When running the wind-tunnel, the fan is constantly adding kinetic energy to the 'closed' system. Energy which through viscous dissipation eventually will become heat. This heat has to be removed at the same rate as it is added if a constant flow temperature is desired in the experiment. In order to do so a heat exchanger, consisting of a car radiator (VW Golf II), was built into the wind-tunnel circuit. In the heat exchanger the cooling medium is tap water. No automatic temperature control system has been implemented as the temperature variations proved to be small enough for optical measurement techniques without automatic control.

After the heat exchanger the cross section shape is gradually changed from rectangular to circular with 400 mm diameter. This is done in a 650 mm long transformer section manufactured in glass fiber reinforced epoxy molded on a plug which was formed from a block of styrofoam using a hot-wire saw.

The return channel is made of standard 400 mm diameter ventilation pipes and standard 90° bends. The total length of the return channel is approximately 12 m and five 90° bends were used. The return channel is supported by consoles bolted to the ceiling. The return channel ends approximately 50 mm before the inlet of the fan in order to have a point in the wind-tunnel circuit with a constant reference pressure (the pressure in the laboratory) and thus avoid pulsating pressures from appearing. The last bend of the return channel has two connectors for hoses one for introducing seeding particles and one for returning the air from the boundary layer suction (see section 2.5).

## 3. Calibration

The wind-tunnel was first built without the return channel and preliminary tests using pitot-tubes and LDV were made in this configuration mainly with the aim to evaluate the inflow conditions and the two-dimensionality of the flow.

### 3.1. *Pitot-tube measurements of the inflow*

Pitot tube measurements of inlet velocity profiles were performed at six different spanwise positions 100 mm upstream of the first corner of the diffuser in order to evaluate the turbulent channel inflow and the spanwise homogeneity of the inflow. In order to reduce the perturbation of the flow, the pitot tube was positioned at the end of a long carbon fiber reinforced sting (see figure 6). The pitot tube was traversed from the wall towards the channel center with a DC servo controlled motor operated from a computer. In order to measure from the opposite wall the sting had to be rotated 180° around its axis. The pitot tube senses the total pressure, the static pressure was measured in a hole on the plane wall and the pressure difference was measured with a Furness Control FCO 510 differential pressure transducer with an accuracy of 0.25% of full scale (2000 Pa). Although the sting had been stiffened by carbon fibers the pitot-tube vibrated during the measurements with an estimated amplitude of 1 mm, this in combination with the rather large 'probe volume' of a pitot tube introduce some uncertainties in the measured data. Small differences in the shapes of the static pressure holes is another error source.

Figure 7 shows the six measured inlet profiles compared to DNS-data by Kim *et al.* (1987) at $Re_\tau = 590$. The DNS-data have been scaled so that the centerline velocity is 22 m/s. Table 2 shows the maximum velocities measured at the six positions. The spanwise positions are measured from the centerline of the diffuser and the positive direction is upwards in the experimental setup. The y-coordinates of the half profiles measured from each side has been matched so that their maximum velocities are at the channel center line. The qualitative shape of the profiles agrees well with the DNS-data. The centerline velocities are varying with a few percent over the whole spanwise width. It should be noted that these measurements where taken before the velocity control, described in section 3.3, was implemented and that the different profiles where measured at different times.

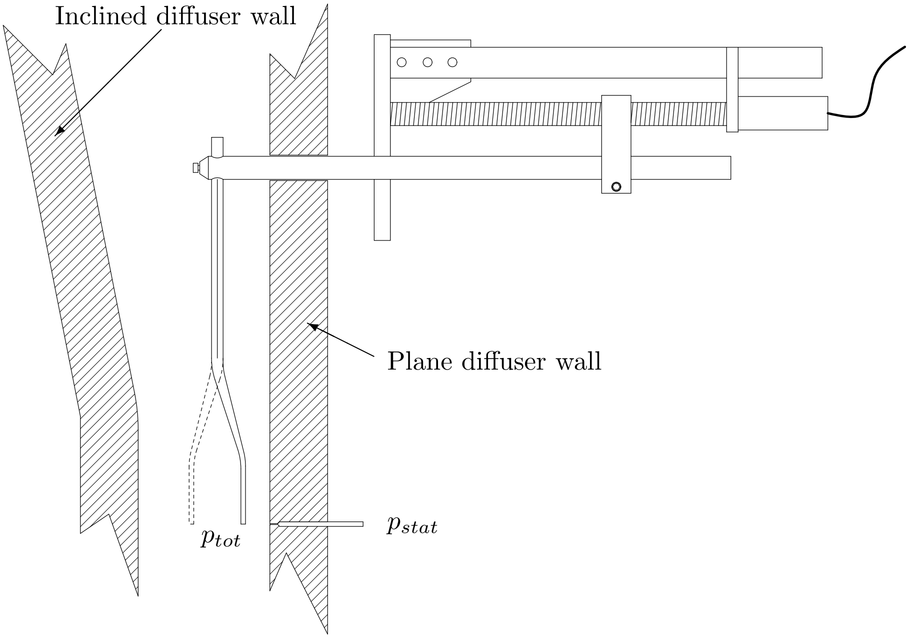

FIGURE 6. Sketch of the setup used for the pitot-tube measurements.

| Spanwise position [mm] | 700 | 400 | 100 | -100 | -400 | -700 |
|---|---|---|---|---|---|---|
| Centerline velocity [m/s] | 22.1 | 22.3 | 22.0 | 22.0 | 22.4 | 22.0 |

TABLE 2. Centerline velocities at the inlet.

### 3.2. *Two-dimensionality*

The previous section concerned the spanwise homogeneity of the inflow but the largest difficulty of this experiment is to get a two-dimensional flow in the adverse pressure gradient region in the diffuser. The methods used to prevent end wall separation are described in 2.5. In order to see if the end wall flow really is attached tufts taped to the end walls were used. With the boundary layer suction turned on, the only backflow that could be observed on the end walls was in the regions where the 'desired' separation is located *i.e.* near the downstream half of the inclined wall and on a limited area downstream of that. Notable is that if the boundary layer suction was turned of, very large scale vortices, which were visualized with smoke, formed. These large vortices could extend 1/3 of the spanwise width from the end walls towards the center line and would probably give rise to a significant flow rate increase in the downstream parts of the diffuser if measurements were taken along the diffuser centerline.

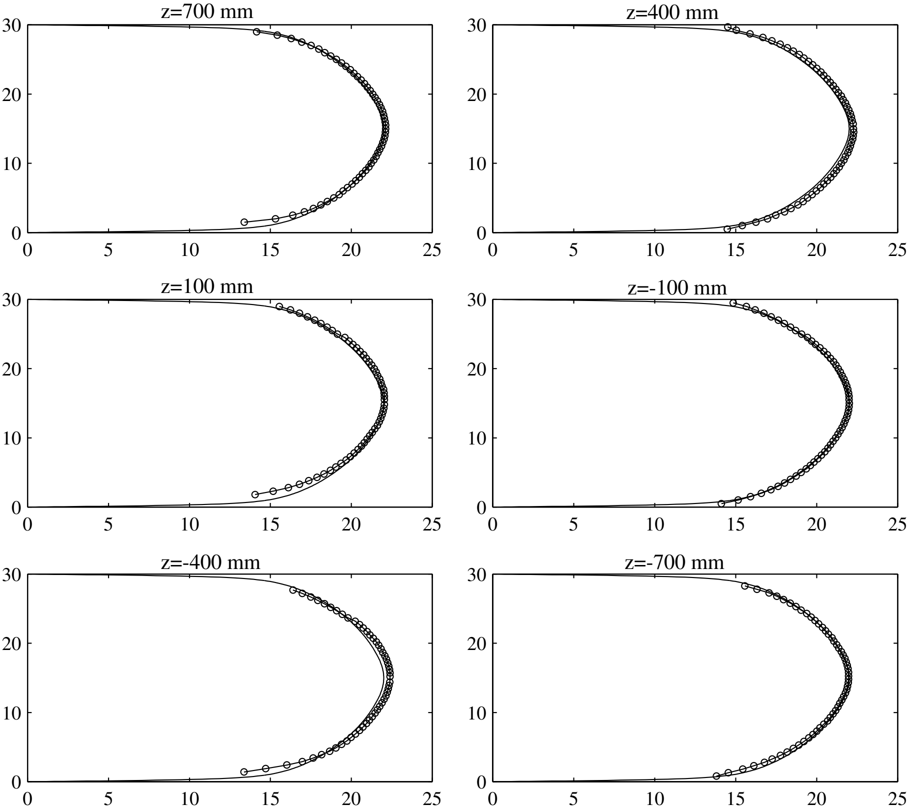

FIGURE 7. Inlet profiles from six spanwise positions compared to DNS-data at $Re_\tau = 590$ by Kim *et al.* (1987). The horizontal scale is velocity in m/s and the vertical scale is wall normal distance in mm.

The flow-rate is a good measure of the two-dimensionality of a flow and for this flow a suitable definition of the flow rate is

$$\frac{1}{HU_b}\int U(y)\mathrm{d}y. \tag{7}$$

Where $U$ is the velocity in the $x$-direction, H is the inlet channel height and $U_b$ is the bulk velocity of the inlet channel flow (*i.e.* $U_b = \int U_{inlet}\mathrm{d}y/H$). Figure 8 shows the flow rate measured with PIV (see Lindgren *et al.* (2002)) in the center region of the measurement section. For comparison the flow rates of Obi *et al.* (1993) and Buice & Eaton (1997) (the data have been taken from Kaltenbach *et al.* (1999)) have been included in the figure. The bulk velocity used for normalization was calculated using equations 1 and 2 and the friction

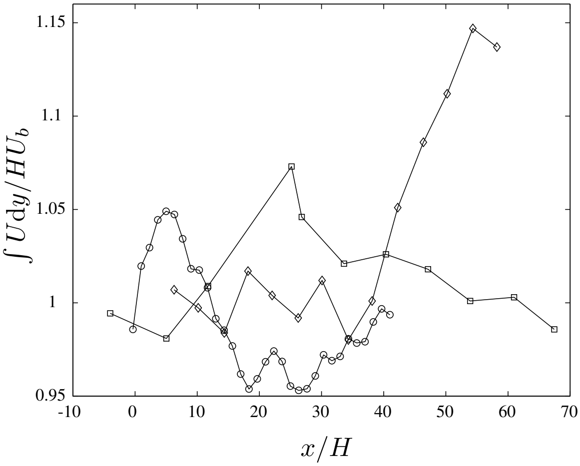

FIGURE 8. Flow rate measured with PIV (○) compared to measurements by Obi *et al.* (1993) (◇) and Buice & Eaton (1997) (□).

velocity at the inlet was measured with a Preston tube. The PIV-data show a peak at $x/H$ around 5 with 5 % higher flow rate as compared to the inlet bulk flow, and after that a decrease to around 3 % lower flow rates.

### 3.3. *Long time velocity variations*

It was noticed when the first measurements with LDV were taken that the mean values of the measured velocity converged very slowly indicating some very long timescale variation, or drift, of the velocity. In order to handle this problem a LabView program (see figure 9) was built allowing the fan to be controlled from the computer. The LabView program measures the air temperature in the wind-tunnel with a PT-100 temperature sensor, the friction velocity at the inlet with a Preston tube connected to a Furness Control FCO 510 differential pressure transducer and the ambient pressure with an absolute pressure transducer connected to the FCO 510. From the measured data the density and viscosity of the air is calculated. These values are used to calculate $Re_\tau$ at the inlet and a proportional controller adjusts the fan speed to keep $Re_\tau$ at a constant level. Figure 10 illustrates the effect of the controller, the control is turned off after 4800 s and turned on again after 70800 s.

## 4. Concluding remarks

An experimental setup for studying the flow in an asymmetric diffuser has been built and verified. The two-dimensionality and the long time velocity variation was given special attention in the wind-tunnel design and evaluation. The

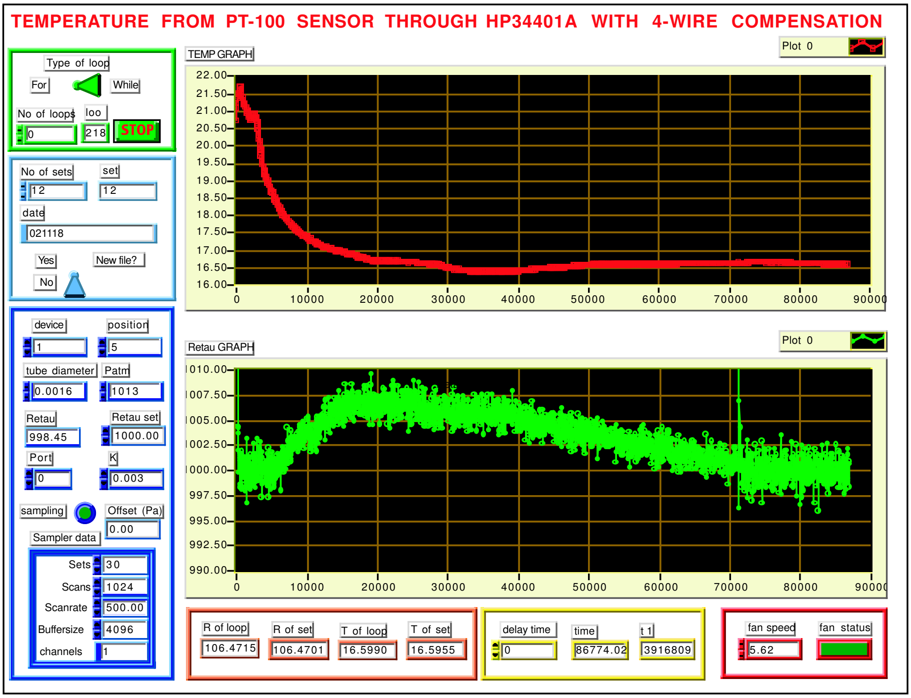

No of loops 0
loo 218
No of sets 12
set 12
date 021118
device 1
position 5
tube diameter 0.0016
Patm 1013
Retau 998.45
Retau set 1000.00
Port 0
K 0.003
Offset (Pa) 0.00
Sets 30
Scans 1024
Scanrate 500.00
Buffersize 4096
channels 1
R of loop 106.4715
R of set 106.4701
T of loop 16.5990
T of set 16.5955
delay time 0
time 86774.02
t 1 3916809
fan speed 5.62
fan status

FIGURE 9. Screen dump from the wind-tunnel control program.

diffuser was designed in such a way that the angle of the inclined wall can be altered between 8° and 10°.

The design of a compact-length transformer between the fan outlet and the inlet channel was successful. Screens, including one bent screen, and splitter plates where used in the transformer in order to expand the flow over a short distance. The inlet channel was designed to be long enough and wide enough to have a fully developed two-dimensional channel flow. The channel flow mean velocity profiles are verified by comparing measurements with DNS data and the spanwise homogeneity is checked by taking measurements at six different spanwise positions.

The two-dimensionality is evaluated by measuring the flow rate in a two-dimensional plane using PIV. The flow rate is found to be constant through the measurement section within ±5%.

The wind-tunnel is controlled from a computer program, logging the atmospheric pressure, the temperature and the friction velocity at the inlet. A controller adjusts the fan speed to keep the inlet Reynolds number constant, a necessary condition for experiment repeatability.

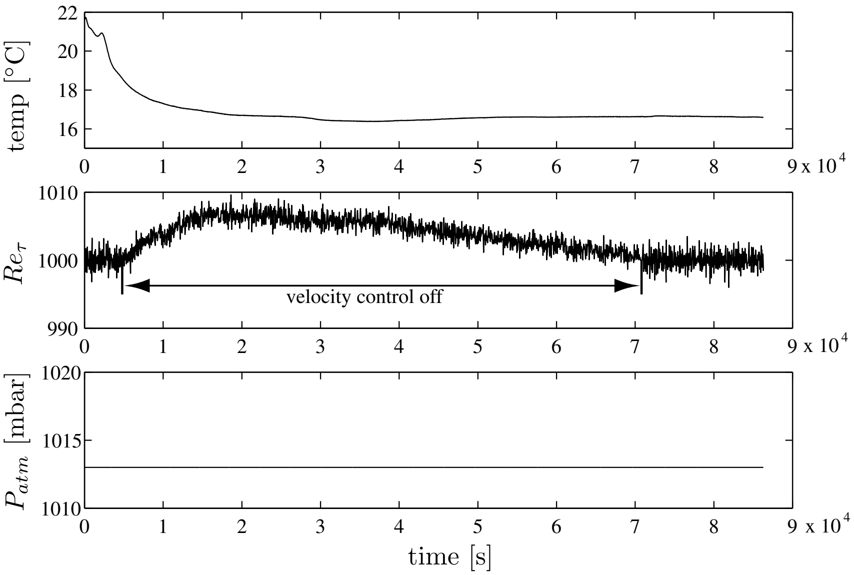

FIGURE 10. Output information from the velocity control program illustrating the effect of velocity control.

## 5. Acknowledgement

The authors would like to thank Ulf Landén for aiding in the manufacturing of the wind-tunnel and measurement equipment. The Swedish Research Council and The Swedish Energy Agency are gratefully acknowledged for their financial support.

## References

ANGELE, K. P. 2002 Pressure-based scaling in a separating turbulent APG boundary layer. In *Advances in turbulence IX* (ed. I. Castro, P. E. Hancock & T. G. Thomas), pp. 639–642. CIMNE, Barcelona, Spain.

BUICE, C. U. & EATON, J. K. 1997 Experimental investigation of flow through an asymmetric plane diffuser. *Tech. Rep.*. Department of mechanical engineering, Stanford university.

CHERRY, N. J., HILLIER, R. & LATOUR, M. E. M. P. 1984 Unsteady measurements in a separated and reattaching flow. *J. Fluid Mech.* **144**, 13–46.

CHITHAMBARAN, V. K., ASWATHA, P. A. & CHANDRASEKHARA SWAMY, N. V. 1984 Mean velocity characteristics of plane diffuser flows with inlet velocity distortion. *J. Indian Inst, Sci.* **65(A)**, 79–93.

COMTE-BELLOT, G. 1965 Écoulement turbulent entre deux paroix parallèles. Publications scientifiques et techniques 419. Ministère de l'air, 2, Avenue de la Porte-d'Issy, Paris.

DIANAT, M. & CASTRO, I. P. 1991 Turbulence in a separated boundary layer. *J. Fluid Mech.* **226**, 91–123.

ETHERIDGE, D. W. & KEMP, P. H. 1978 Measurements of turbulent flow downstream of a rearward-facing step. *J. Fluid Mech.* **86**, 545–566.

JOHANSSON, A. V. & ALFREDSSON, P. H. 1982 On the structure of turbulent channel flow. *J. Fluid Mech.* **122**, 295–314.

JOHANSSON, A. V. & ALFREDSSON, P. H. 1986 Structure of tubulent channel flows. In *Encyclopedia of Fluid Mechanics*, chap. 25, pp. 825–869. Gulf publishing company.

KALTENBACH, H.-J., FATICA, M., MITTAL, R., LUND, T. S. & MOIN, P. 1999 Study of flow in a planar asymmetric diffuser using large-eddy simulation. *J. Fluid Mech.* **390**, 151–185.

KIM, J., MOIN, P. & MOSER, R. 1987 Turbulence statistics in fully developed channel flow at low Reynolds number. *J. Fluid Mech.* **177**, 133–166.

LAWS, E. & LIVESEY, J. 1978 Flow through screens. *Ann. Rev. Fluid Mech.* **10**, 247–266.

LINDGREN, B. & JOHANSSON, A. V. 2002 Design and evaluation of a low-speed wind-tunnel with expanding corners. Technical report ISRNKTH/MEK/TR–02/14-SE. Dept. of mechanics, KTH.

LINDGREN, B., TÖRNBLOM, O. & JOHANSSON, A. V. 2002 Measurements in a plane asymmetric diffuser with 8.5° opening angle. part I: General flow characteristics. *To be submitted* .

OBI, S., AOKI, K. & MASUDA, S. 1993 Experimental and computational study of turbulent separating flow in an asymmetric plane diffuser. In *Ninth Symp. on Turbulent Shear Flows*, p. 305. Kyoto, Japan.

PERRY, A. E. & FAIRLIE, B. D. 1975 A study of turbulent boundary-layer separation and reattachment. *J. Fluid Mech.* **69**, 657–672.

RUDERICH, R. & FERNHOLZ, H. H. 1975 An experimental investigation of a turbulent shear flow with separation, reverse flow, and reattachment. *J. Fluid Mech.* **163**, 283–322.

SOVRAN, G. & KLOMP, E. D. 1967 Experimentally determined optimum geometries for rectelinear diffusers with rectangular, conical, or annular cross-section. In *Fluid mechanics of internal flow* (ed. G. Sovran), pp. 270–319. Elsevier publishing company.

TAYLOR, G. & BATCHELOR, G. K. 1949 The effect of wire gauze on small disturbances in a uniform stream. *Quart. J. Mech. and App. Math.* **2**, part 1,1.

YOSHIOKA, S., OBI, S. & MASUDA, S. 2001 Turbulence statistics of periodically perturbed separated flow over backward facing step. *Int. J. of Heat and Fluid Flow* **22**, 391–401.